Active site geometry stabilization of a presenilin homolog by the lipid bilayer promotes intramembrane proteolysis

Lukas P. Feilen[1], Shu-Yu Chen[2], Akio Fukumori[3], Regina Feederle[1,4], Martin Zacharias[2], Harald Steiner[1,5,*]

[1]German Center for Neurodegenerative Diseases (DZNE), Munich, Germany

[2]Physics Department T38, Technical University of Munich, Garching, Germany

[3]Department of Pharmacotherapeutics II, Faculty of Pharmacy, Osaka Medical and Pharmaceutical University, Takatsuki, Japan

[4]Institute for Diabetes and Obesity, Monoclonal Antibody Core Facility, Helmholtz Munich, German Research Center for Environmental Health, Neuherberg, Germany

[5]Biomedical Center (BMC), Division of Metabolic Biochemistry, Faculty of Medicine, LMU Munich, Germany

*Correspondence: harald.steiner@med.uni-muenchen.de

Keywords

Amyloid β-peptide, intramembrane proteolysis, presenilin, PSH, γ-secretase

ABSTRACT

Cleavage of membrane proteins in the lipid bilayer by intramembrane proteases is crucial for health and disease. Although different lipid environments can potently modulate their activity, how this is linked to their structural dynamics is unclear. Here we show that the carboxy-peptidase-like activity of the archaeal intramembrane protease PSH, a homolog of the Alzheimer´s disease-associated presenilin/γ-secretase is impaired in micelles and promoted in a lipid bilayer. Comparative molecular dynamics simulations revealed that important elements for substrate binding such as transmembrane domain 6a of PSH are more labile in micelles and stabilized in the lipid bilayer. Moreover, consistent with an enhanced interaction of PSH with a transition-state analog inhibitor, the bilayer promoted the formation of the enzyme´s catalytic active site geometry. Our data indicate that the lipid environment of an intramembrane protease plays a critical role in structural stabilization and active site arrangement of the enzyme-substrate complex thereby promoting intramembrane proteolysis.

INTRODUCTION

Intramembrane proteolysis is a crucial cellular mechanism underlying many fundamental physiological processes [1,2]. It is also involved in pathological conditions, most prominently in Alzheimer´s disease (AD). Here, intramembrane cleavage within the transmembrane domain (TMD) of the amyloid precursor protein (APP) derived C99 substrate by γ-secretase results in the release of a variety of amyloid β-peptide (Aβ) species [3]. The longer forms, Aβ42 and Aβ43, are toxic to neurons and believed to trigger the onset of AD [4]. γ-Secretase is a membrane-embedded protein complex consisting of four components [5]. The catalytic subunit presenilin is an aspartyl intramembrane protease [6-10] present in the mammalian γ-secretase complexes as either presenilin-1 (PS1) or presenilin-2 variant [11,12]. Mutations in PS1 are the major cause of familial AD (FAD) and cause an imbalance in the production of Aβ species that leads to relative increases of the longer forms over the normally major form Aβ40 [3]. Presenilins are evolutionary highly conserved proteins and related to the signal peptide peptidase (SPP) [13] family of intramembrane proteases [14]. Ancestral precursors of presenilin and SPP exist in several archaea [15] and share key signature motifs including the protease family-defining GxGD active site motif with presenilin and SPP [8]. The archaeal homolog from *Methanoculleus marisnigri* JR1 termed presenilin/SPP homolog (PSH) is capable of cleaving C99 and several other substrates [15-18]. Similar to presenilin in the γ-secretase complex, PSH appears to cleave C99 in a sequential manner starting by initial ε-site cleavages between L49 and V50 (ε49) or T48 and L49 (ε48) followed by the release of various Aβ species from stepwise carboxy-terminal trimming cleavages [16,19]. However, in contrast to presenilin, which requires complex formation with the other γ-secretase complex components for activity [20-22], PSH is active without accessory components. The crystal structure of PSH revealed first important insights into aspartyl intramembrane

proteases showing that the two catalytic aspartate residues of the active site in TMD6 and TMD7 directly face each other and locate in a water-accessible cavity [23]. Subsequent cryo-electron microscopy (cryo-EM) structural analysis of γ-secretase showed that presenilin adopts a structure in the complex very similar to that of PSH [24] with nearly identical positions of the catalytic residues [25]. Further cryo-EM studies showed that binding of APP and Notch substrates causes major conformational changes in both enzyme and substrate [26,27]. These led to an enzyme-substrate complex (E-S) with an extended TMD6 by formation of a new and stable TMD6a helix as well as a hybrid β-sheet between enzyme and substrate that causes unfolding of the ε-cleavage site region in the substrate [26,27]. Interestingly, formation of the TMD6a helix was also observed by cryo-EM upon inhibitor binding thus partially mimicking the substrate-bound state [28,29].

The very similar structural folds of presenilin and PSH and the ability to cleave C99 in the TMD at the same sites as γ-secretase [15,16] make PSH an attractive model for the intrinsic protease activity of presenilin. To gain basic insights into the enzymatic workings of presenilin proteases, we thus set out to characterize the influence of two fundamentally different hydrophobic environments on the activity of PSH and asked if cleavage of C99 by the solubilized enzyme in detergent micelles would differ from a lipid-reconstituted state and if so, whether such differences could be correlated with the structural dynamics of this prototype presenilin protease or its E-S. Although the influence of lipids on the activity of presenilin and other intramembrane proteases is well documented [30], there are so far no studies in which biochemically determined activities of these proteases were linked with structural information that could explain how lipids, in particular a membrane bilayer environment, affect intramembrane protease structural dynamics and enzyme function. Since presenilins are not active in detergent micelles without lipids [31] this

critical question can however not be addressed for γ-secretase directly and requires a suitable model protease such as PSH. We found that detergent-solubilized PSH has a reduced carboxy-terminal trimming activity, i.e. processivity, compared to γ-secretase giving rise to an increased production of very long Aβ species such as Aβ46. Strikingly, the reconstitution of PSH into a lipid bilayer strongly promoted the protease processivity to shorter Aβ species such as Aβ38 highlighting the important role of the lipid membrane environment for intramembrane proteolysis. Furthermore, it enhanced the binding of a transition-state analog (TSA) γ-secretase inhibitor (GSI) affinity probe suggesting a more stable active site conformation in the lipid bilayer. These biochemical studies were accompanied by comparative modeling and molecular dynamics (MD) simulations to study the effect of detergent micelle and membrane lipid environment on substrate-bound PSH. In good agreement with the experimental data, the computational data suggest that the stabilization of TMD6a and the active site can explain the increased processivity and inhibitor binding in the membrane bilayer. Mutational analysis confirmed the assumed critical functional role of β-sheet and TMD6a corroborating the computational analysis of substrate-bound PSH. Collectively, these data provide insights into how structural adaptations occurring in response to changes in the hydrophobic environment from a micellar membrane mimetic to a real lipid bilayer translate into activity changes of an intramembrane protease. Moreover, with general implications for intramembrane proteolysis, they show how a lipid bilayer allows the formation of a stabilized active site geometry poised for substrate cleavage.

RESULTS

PSH cleaves APP C99 to longer Aβ species

To get insights into the intrinsic protease activity of presenilin, we set out to further characterize the intramembrane cleavage of C99 by PSH (**Figure 1A**). Consistent with previous findings [16], n-dodecyl β-D-maltoside (DDM)-solubilized, His-affinity-purified PSH could cleave the C99-based APP C100-His_6 substrate [21] as demonstrated by the generation of the APP intracellular domain (AICD) and Aβ cleavage products (**Figure 1B**). Cleavage was inhibited by the TSA GSI L-685,458 [32] (**Figure 1B**) although much higher, micromolar concentrations were needed for efficient inhibition compared to those known for γ-secretase [7,32]. Analysis of the Aβ profile using Tris-Bicine urea SDS-PAGE (**Figure 1C**) and MALDI-TOF mass spectrometry (**Figure 1D, Figure 1 – figure supplement 1**) showed that Aβ40 and Aβ42 were the major Aβ species produced with a preference of Aβ42 over Aβ40. Interestingly, besides the increased generation of Aβ42 even longer Aβ species such as Aβ46 were relatively abundant. This suggests that PSH cleaves C99 at the same sites as γ-secretase but with reduced processivity.

Lipid membrane enhances the processivity of PSH

We next investigated how a membrane environment of PSH influences the cleavage and processivity of the protease. Previous studies have shown that γ-secretase activity is dependent on the membrane environment as modulations of the lipid composition and/or bulk membrane properties in cell-free assays affected total activity as well as the ratios of the Aβ species generated [33-36]. Furthermore, it was also shown that varying the pH in cell-free assays can modulate the total activity as well as the processivity of γ-secretase [37]. To investigate whether and how PSH cleavage of C99 would respond to a change from the micellar environment in DDM to a lipid bilayer environment, PSH was reconstituted in defined small unilamellar vesicles (SUVs) composed of palmitoyl-oleoyl PC (POPC), the most abundant

phospholipid of biological membranes (**Figure 2 – figure supplement 1A, B**). We then performed PSH *in vitro* assays with DDM-solubilized or POPC-reconstituted PSH in a pH range from 5.5 to 9.0. As shown in **Figure 2A**, the total activity was highest in the mild acidic to mild alkaline pH range and sharply dropped at pH values above 8.0. The pH optima for both conditions were very similar and lying around pH 7.0. However, compared to the DDM-solubilized enzyme, the processivity of PSH was strongly promoted in the lipid bilayer environment of the POPC SUVs as seen by a strongly increased production of Aβ38 and Aβ40 and the strong reduction of longer Aβ species (**Figure 2B**). Interestingly, the processivity of the reconstituted PSH appeared to be more reduced at alkaline pH values as judged from the appearance of Aβ species longer than Aβ42 (**Figure 2B**) at pH 7.5 and higher. A direct comparison of the Aβ profiles at pH 7.0 confirmed the increased processivity of PSH in the POPC lipid bilayer (**Figure 2C, Figure 2 – figure supplement 2A**). Finally, we investigated the initial ε-site cleavages of C99 by PSH in DDM micelles or POPC vesicles at this pH. Mass spectrometry analysis showed that C99 was cleaved in both conditions at the ε49 and ε48 cleavage sites resulting in the release of the two N-terminally distinct AICD50 (ε49) and AICD51 (ε48) species (**Figure 2D**, **Figure 2 – figure supplement 2B**). Collectively, these data show that the lipid environment increases the processivity of PSH in cleaving C99.

Enhanced processivity of PSH is independent of the APP substrate N-terminus

Since the activities of DDM-solubilized and reconstituted PSH clearly differed, particularly in the processivity, we next sought to understand the underlying basis for this behavior at the level of its structural dynamics. Since there is no structure of PSH in complex with C99 available and structural investigations on γ-secretase in complex with an APP substrate were so far only performed with C83, an N-terminally

171 shorter alternative C-terminal APP fragment generated by α-secretase [38], we first
172 tested whether C83 is processed similarly than C99. We thus analysed its cleavage
173 by PSH in DDM micelles and the POPC bilayer at pH 7.0. C83 was cleaved by PSH
174 in both conditions resulting in the generation of an AICD and the Aβ-equivalent
175 cleavage product p3 [38] (**Figure 3A**). As judged from the processivity-reflecting ratios
176 of p3 species ending at position 40 and 42, in contrast to the DDM micelle
177 environment, the POPC bilayer enhanced the processivity and caused an increase in
178 the relative production of shorter p3 species (**Figure 3B**). The increase in
179 processivity was similar to that observed under these conditions for the
180 corresponding Aβ species produced from C99 (**Figure 3C**). These data show that
181 the increased processivity in the POPC environment is independent of the N-
182 terminus of the substrate and that C83 and C99 behave comparable in both
183 environments, so that C83 should be suitable as C99 surrogate for structural
184 modelling and molecular dynamics simulations of PSH in complex with a substrate
185 using information from the C83-bound γ-secretase.
186
187 **Structural modeling shows key features of substrate-bound γ-secretase in PSH**
188 Since no experimental structure of the substrate-bound (holo) PSH is available, we
189 generated 3 different starting structures, model 1, 2 and 3, for the PSH holo form
190 using template-based modeling by assuming that PSH binds its substrate in a similar
191 way as PS1. Since the PSH crystal structure [23] (PDB 4HYG) misses several
192 residues and loop segments in its substrate-free (apo) form, it is necessary to include
193 the cryo-EM structure of holo PS1 bound to the C83 γ-secretase substrate [26] (PDB
194 6IYC) as an additional template. In model 1, we used the entire holo PS1 including
195 the C83 substrate as template whereas in model 2 and 3 most of the apo PSH
196 structure was included and only different parts of missing loops segments were

197 modelled based on the 6IYC template (including the C83 substrate, see Materials
198 and Methods for details). The overall structures of our holo PSH models are close to
199 the experimentally determined apo PSH crystal structure [23] but include several
200 residues and loop segments that are missing in the apo crystal structure (**Table 1,**
201 **Figure 4 – figure supplement 1A, B, Figure 4 – figure supplement 2**). In
202 particular, as exemplified for model 2 (**Figure 4A**), it includes the TMD6a helix
203 (residues H171-E177) C-terminal of TMD6 and the hybrid β-sheet formed between
204 the β2-strand (A213-G217) and the β3-strand (V50-K54) of the substrate, which is
205 stabilized by backbone interactions with residue Q272 preceding TMD9 (**Figure 4B**).
206 These two structural elements were also found in the γ-secretase complexes with
207 bound C83 [26] or Notch1 [27] (PDB 6IDF) and were not present in the substrate-free γ-
208 secretase complex. In addition, a salt bridge between R70 and E181 in the
209 homology-modeled PSH (**Figure 4C**) replaced the hydrogen bond partners Y159 and
210 R278 of the substrate-bound γ-secretase structure (**Figure 4D**). Thus, key features
211 for substrate interaction (TMD6a and hybrid β-sheet) known from the γ-secretase–
212 substrate complexes are analogously found in our models of the PSH–C83 complex.
213
214 **Verification of β2-strand in the substrate-bound PSH models**
215 Comparative modeling is sensitive to the choice of the templates and how the
216 sequences are aligned together. A template with low quality or a sequence
217 alignment with high uncertainties can lead to an unrealistic protein structure.
218 Therefore, it is necessary to verify the presence of specific structural features in our
219 substrate-bound PSH models that were observed in the substrate-bound PS1
220 structure. In case of γ-secretase, the deletion of the β2-strand (R377-L381) impaired
221 the activity of the enzyme towards C83 and Notch1 [26,27]. To investigate whether this
222 structural element is of similar functional importance in PSH, we mutated amino acid

residues A213, F214 and V215 within the putative PSH β2-strand to prolines. Similar as done for PS1 [26,27], we also deleted amino acid residues A213 to M216 and A213 to G217. When assessed for their enzymatic activity, the three mutants as well as the two deletion constructs showed clearly, and mainly strongly, decreased activities compared to wild type (WT) PSH in both DDM micelle or POPC bilayer conditions (**Figure 4E**). These results suggest that as the residues 213 to 216/217 are important for the activity of the protease they might indeed form the β2-strand observed in our structural models.

Comparative molecular dynamics simulations of PSH in micelle and membrane environment reveals reduced PSH flexibility in the lipid bilayer

To get insight into the molecular details on how micelle and membrane environments might influence PSH conformational dynamics, the constructed C83-bound PSH models were embedded in DDM micelle (150 DDM molecules) or POPC bilayer (302 POPC molecules) environments and in each case three simulations with different distribution of starting velocities were performed (each simulation length: 0.6 μs). In total, 6 systems were constructed and 18 trajectories were generated *in silico*.

Snapshots of the PSH holo form in both environments are shown for model 2 in **Figure 5A**. All simulated systems stayed overall close to the starting structures with root-mean-square deviations (RMSD) relative to the start structure of about or less than 4.0 Å and an overall lower RMSD for all model 2 simulations (**Figure 5 – figure supplement 1A**). Larger deviations were observed for all model 1 simulations and for one trajectory for model 3. It is likely that model 1 is less realistic than model 2 and 3 because it is entirely based on the PS1 template structure and is missing structural information from PSH.

We first analyzed the substrate mobility and interaction with PSH during the simulations in both environments. Stable substrate binding near the active site region involves the interaction of the β2-strand with the β3-strand at the C-terminus of the C83 substrate, which is required for substrate cleavage. The overall β-sheet interaction in terms of hydrogen bonds (H-bonds) was found to be similar in both the micelles and membrane environments except for model 3 where the H-bonds are more frequently formed in the bilayer (**Figure 5B**). We next investigated the mobility of the individual residues of C83 and PSH by calculating the root-mean-square fluctuation (RMSF) as well as the water accessibility of residues in the C83 substrate TMD by counting the average number of water molecules within 5 Å of the residue of interest. Both RMSF and water accessibility for each amino acid were not much different in both environments (**Figure 5C, D**). Notably, the substrate remained in a dry region from G37 to V46 and abruptly gained an increase in water accessibility around T48 and L49, which correspond to the initial ε-cleavage sites of C83 (and C99).

To quantitatively evaluate the flexible regions of PSH, RMSF profiles of each residue along the PSH sequence were calculated (**Figure 5E**). In all three models, larger fluctuations of hydrophilic loop 1 (HL1, between TMD1 and 2) were observed in DDM compared to POPC (**Figure 5E**). Similarly, the atomic fluctuations of TMD6a in model 1 and 2 were reduced in POPC versus DDM but no differences in the two environments were observed for TMD6a in model 3. In both environments, the atomic fluctuations of residues C-terminal of TMD6a stayed reduced in model 1 while they increased in model 3. In contrast to models 1 and 3, the atomic fluctuations of these residues stayed reduced in POPC and increased in DDM in model 2 (**Figure 5E, Figure 5 – figure supplement 1B**). Furthermore, secondary structure analysis showed that TMD6a is mostly unfolded in model 1 and stable in model 3 (**Figure 5 –**

figure supplement 2A, C). Strikingly, when model 2 is placed in the micelle environment, TMD6a of substrate-bound PSH underwent a conformational transition between an α-helix and a loop structure (**Figure 5 – figure supplement 2B**), while this transition was not observed for TMD6a in the POPC bilayer showing that the membrane environment stabilizes TMD6a (**Figure 5 – figure supplement 2B**).

Despite the high structural similarity between the starting structures of model 2 and model 3 (RMSD = 0.163, **Figure 4 – figure supplement 1B**), a difference in TMD6a positioning was observed during the simulations of these two models in the POPC environment. While TMD6a is located closer to C83 in model 2, it is located further away from C83 in model 3 (**Figure 5 – figure supplement 3A**). In addition, when we directly compared the RMSF profiles of models 2 and 3 (**Figure 5E**) with each other, we observed that the residues immediately C-terminal of TMD6a are slightly more mobile in model 3 (**Figure 5 – figure supplement 3B, C**). Because these residues are spatially close to HL4 between TMD4 and TMD5, HL4 also becomes more flexible in model 3 (**Figure 5 – figure supplement 3B**). In fact, the conformational discrepancy in these regions arise from the model building of the two models which were built differently for residues A163 to R193 and E210 to G219 (**Table 1,** see Materials and Methods for details). With a closer contact between TMD6a and C83 as well as an overall lower RMSD for model 2, we justified that model 2 may describe the dynamics of the PSH-C83 complex best so that model 2 is, therefore, mainly used for our following analysis.

DDM insertion leads to an unwinding of PSH TMD6a

The biochemical cleavage data as well as the fluctuations in the MD simulations indicate a potential weakening of the E-S interaction in the micelle environment. This might explain the remarkable shift in processivity of PSH in the presence of a

membrane lipid bilayer. In our PSH models, TMD6a creates a hydrophobic patch (formed by residues M172, I173, L175 and A176) that contacts the C83 substrate in the ε-cleavage site region (e.g. V50 and L52, **Figure 6A**). Similar interactions are found in the experimentally resolved C83-bound and Notch1-bound γ-secretase structures [26,27], as well in the GSI-bound γ-secretase structures [29] (**Figure 6 – figure supplement 1A-D**). To gain a more detailed mechanistic view on how DDM and POPC molecules modulate the E-S stability, we calculated the structural properties of these molecules. Furthermore, we investigated how these molecules interact with PSH and C83. In the bilayer environment, the simulations indicate that POPC molecules are well ordered as indicated by a high lipid order parameter S_{CH} (**Figure 6 – figure supplement 2A, B**) and the computed area per lipid of ~ 68 $Å^2$ is close to the experimentally determined value of 64.3 $Å^2$ [39] (**Figure 6 – figure supplement 2C**). In contrast, in the micelle environment, DDM molecules are more mobile and can change their orientation more freely, as indicated by the lower lipid order parameter S_{CH} for DDM compared to POPC (**Figure 6 – figure supplement 2A, B**). In a larger micelle environment, with 50% more DDM molecules (225 DDM molecules, **Figure 6 – figure supplement 3A**) the lipid order parameter of DDM improved (**Figure 6 figure supplement 3B**). Nevertheless, the number of H-bonds in the β-sheet (**Figure 6 – figure supplement 3C**), the RSMF profile (**Figure 6 – figure supplement 3D**) and the water accessibility in the C83 substrate (**Figure 6 – figure supplement 3E**) did not differ from the respective values in the smaller DDM micelle (150 DDM molecules). The atomic fluctuations also did not differ largely between the different micelle sizes except for strongly reduced fluctuations of HL1 in the larger micelle (**Figure 6 – figure supplement 3F**) originating from the more ordered DDM molecules around HL1 (**Figure 6 – figure supplement 3H**). Furthermore, TMD6a and residues C-terminal of TMD6a were found to be also flexible in the larger DDM

micelle as observed for the smaller micelle (**Figure 6 – figure supplement 3F, G**), indicating that the size of the DDM micelle does not influence the observed differences in flexibility of TMD6a between DDM and POPC environment.

Although most of the DDM molecules are well aligned to the membrane normal at the protein periphery, some can transiently flip to a direction perpendicular to the membrane normal near to the gaps between TMDs (such as TMD2-TMD6 and TMD3-TMD4) (**Figure 6B-D, Video 1 and Video 2**). When inserted into the intramolecular gaps between TMD2 and TMD6, the DDM molecule perturbs intramolecular interactions by forming unspecific hydrogen bonds with the adjacent amino acid backbones, and thus destabilizes TMD6a (**Figure 6B-C**). In addition, DDM inserts between TMD3 and TMD4 of PSH in the micelle environment and interacts with the loop C-terminal of TMD6a, corresponding to the higher RMSF observed for these residues (**Figure 5E, Figure 6D**). In contrast, the well-ordered POPC molecules do not enter into the gaps between TMDs (**Video 3**) and do, therefore, not disturb intramolecular interactions. Collectively, these data suggest that a membrane lipid environment promotes the formation of a stabilized E-S of PSH with the APP C83 substrate by the stabilization of TMD6a, an important structural element involved in substrate stabilization.

Lysine mutations in TMD6a lead to helix unwinding and reduced activity

Our computational results suggest that the TMD6a helix plays an important role for substrate binding of PSH. Furthermore, the residues of the hydrophobic patch in TMD6a (M172, I173, L175 and A176) of PSH correspond to a homologous hydrophobic patch in the TMD6a of PS1 (L271, V272, T274 and A275), which is also affected by FAD mutations [3]. Some of them display a strong loss of function such as L271V and T274R [40] supporting the idea that TMD6a has an important function in

substrate cleavage. To investigate the functional role that TMD6a plays in substrate stabilization, we performed additional MD simulations of *in silico* generated lysine mutations of M172, I173, L175 and A176 in the TMD6a hydrophobic patch in order to disrupt its nonpolar character. Because TMD6a is already unstable in DDM, the simulations were performed in the POPC environment only. The RMSD plots indicate that in most of the simulations, mutated PSH remained in an overall stable structure with RMSDs ~ 3.0 Å (similar to WT) (**Figure 7A**). In addition, no significant difference was found in C83 RMSF (**Figure 7B**), residue-wise water distribution (**Figure 7C**) and the hydrogen-bonding pattern of the β-sheet C-terminal of the ε-cleavage site (**Figure 7D**).

The PSH RMSF plots show that all mutations destabilize TMD6a to different degrees while having only smaller effects in other regions in comparison to WT (**Figure 7E**). It is worth noting that L175K introduces the largest TMD6a fluctuation, compared to the WT and the other three lysine mutants. Nevertheless, all four mutations distorted the helical structure of TMD6a in at least one of the simulations. (**Figure 7 – figure supplement 1**). Finally, to experimentally validate these structural predictions, we analyzed the cleavage of C99 by these mutant forms of PSH. All four mutants showed a strongly decreased, nearly abolished cleavage of C99 compared to WT PSH in both DDM micelle or POPC bilayer conditions (**Figure 7F**) suggesting that TMD6a and its hydrophobic patch is an important structural element of PSH.

Lipid membrane environment stabilizes the active site geometry of PSH

The proteolysis reaction requires a specific geometry of all elements that form the active site. A critical issue is the distance between the two catalytic aspartic acids D162 and D220. Free energy calculation along the distance between D257 and

D385 of PS1 has suggested that mutations disturbing the active site geometry and alter the distance between D257 and D385 correlate with changes in enzyme activity [41]. In PSH, the geometry is characterized by the Cγ-Cγ distances between the D162 and D220. The distances appeared more frequently around 6.8 Å in our model when placed in a bilayer environment (**Figure 8A, Figure 8 – figure supplement 1**). These distances correspond to a potentially catalytically active site geometry that can also accommodate a water molecule between the catalytic aspartates and L49 essential for the proteolytic cleavage (**Figure 8B**). In contrast, larger distances are more frequently sampled in the micelle environment. When the distance is enlarged here, an increased number of water molecules can access the catalytic center and disturb the catalytic geometry (**Figure 8B**). Proteolysis-compatible Cγ-Cγ distances below 7.0 Å were more frequently sampled in the membrane environment (~ 76%) compared to simulations in the DDM environment (~ 63%). Detailed geometries at the catalytic site of the E-S for a smaller and a larger Cγ-Cγ distance are depicted in **Figure 8 – figure supplement 2A, B**.

To experimentally test whether the lipid environment influences the active site geometry of PSH, we used the L-685,458-based biotinylated affinity ligand Merck C [42] to capture PSH in DDM micelles and in POPC vesicles. As shown in **Figure 8C**, Merck C was able to capture specifically PSH as judged from binding competition in the presence of excess amounts of the parental compound L-685,458. In all these experiments, binding competition was stronger in the POPC vesicles than in DDM micelles indicating that the more labile DDM environment also weakens the competition of binding with the parental compound. In addition, also the background level of unspecific binding was higher in the latter environment contributing to the higher levels of unspecific PSH capture. In agreement with these observations, quantitation of specifically Merck C-bound PSH showed that the capture was

markedly enhanced for the protease in the POPC bilayer (**Figure 8D**). Additional enzyme inhibition experiments further showed that both inhibitors, the parental L-685,458 as well as Merck C, inhibited PSH less well in DDM than in POPC (**Figure 8E, F**). All in all, these findings support the interpretation that the POPC bilayer stabilizes the active site, whereas it is destabilized in DDM micelles. Thus, these data suggest that the lipid environment stabilizes the geometry of the active site, which translates into the increased processivity of PSH in POPC vesicles.

Despite the improved binding and capture of PSH by the L-685,458-derived affinity probe in the POPC membrane environment, a potent inhibition of PSH by L-685,458 required rather high micromolar concentrations of this GSI. We thus finally tested whether other known GSIs would be more effective in inhibiting PSH cleavage of C99. Besides L-685,458, another TSA inhibitor (III-31C [43], **Figure 8 – figure supplement 3A, B**) and four non-TSA inhibitors with comparable potency (DAPT [44], LY411575 [45], Begacestat [46] and MRK-560 [47], **Figure 8 – figure supplement 3C-F**) were tested for their potential to inhibit reconstituted PSH at pH 7.0. Remarkably, only the TSA inhibitor III-31C was able to inhibit C99 cleavage by PSH whereas the non-TSA inhibitors were largely ineffective, even when used at the same high concentrations as for L-685,458 (20 μM) (**Figure 8G**). Overall, these inhibition data suggest that the stabilizing interactions of the TSA inhibitors in the PSH active site region may be different from that of γ-secretase [29,48]. Such differences in stabilizing interactions might also affect the other GSIs that may bind too weakly to inhibit the enzyme.

Taken together, the MD simulations indicate a more stable, i.e. less fluctuating, geometry of the enzyme-substrate binding state around the enzyme active site in a POPC membrane environment compared to a DDM micelle environment. The DDM environment appears to destabilize important structural elements such as the TMD6a

that is required for a stable enzyme-substrate interaction. These results can qualitatively explain the experimentally observed reduced processivity of PSH in DDM micelles and its boost in the POPC bilayer. Further, they emphasize the critical importance of the membrane environment for the formation of a conformationally stable active site geometry in the E-S complex, which is key for the efficient operation of intramembrane proteases in general.

DISCUSSION

It has previously been demonstrated that the archaeal intramembrane protease PSH cleaves the APP substrate C99 into Aβ40 and Aβ42 in a manner very similar to γ-secretase [16]. PSH can thus be used as a surrogate for γ-secretase allowing to study the proteolytic activity of its catalytic presenilin subunit in the absence of its complex partners. Here we confirm and extend these prior findings by a further, more in depth characterization of C99 processing by PSH. We first found that detergent-solubilized PSH cleaves C99 in DDM micelles with a reduced processivity as evident from higher amounts of Aβ42 than Aβ40. The reduced processivity of PSH under these conditions was supported by the identification of longer Aβ species such as Aβ46, cleavage products that were not identified in the previous study. Strikingly, we found in our assay system that the processivity was strongly enhanced in a membrane bilayer when the enzyme was reconstituted into POPC SUVs. Under these conditions, PSH processivity was strongly promoted as seen by the increased production of Aβ38. The protease was pH-dependent and showed the highest activity in the mild acidic to mild alkaline pH range in both micelle and bilayer conditions. In the POPC bilayer, the processivity of PSH was increased up to neutral

456 pH before it rapidly dropped in the alkaline pH range of 7.5 – 8.5, where longer Aβ
457 species started to accumulate eventually remaining unprocessed. Although the
458 pH/activity profile of PSH showed overall similarities to that of γ-secretase, there
459 were some notable differences. Compared to γ-secretase, which has a pH optimum
460 of 6.5 [37], that of PSH was shifted to neutral pH. Moreover, although the processivity
461 of γ-secretase was increasingly impaired towards more alkaline conditions like for
462 PSH shown here, paradoxically, relative increases of Aβ38 were observed for γ-
463 secretase in parallel [37]. Clearly, the most remarkable observation, however, was the
464 rise in processivity when PSH was reconstituted into POPC membranes.

465 In searching for the underlying basis of these dramatic activity changes when
466 changing from a micelle to a bilayer environment, we asked if these could be due to
467 potential structural rearrangements that PSH undergoes in these two different
468 environments. To investigate this possibility, PS1-based homology models were
469 generated for PSH in the APP C83 substrate-bound holo form and the substrate-free
470 apo form. The models revealed both β2-strand and TMD6a as structural elements,
471 which we found by mutational analysis to be functionally highly critical for substrate
472 cleavage by PSH. As observed for substrate-bound PS1 [26,27], this suggests that they
473 constitute important structural elements for substrate binding also for PSH.

474 The conformational dynamics of these structural models was evaluated in MD
475 simulations to test whether structural changes might be observable that could explain
476 the activity changes. We note that in previous simulations the atomistic dynamics of
477 γ-secretase and the interaction with C83 have been studied [49,50], including very
478 recently also its activated state poised for ε-site cleavage [50]. However, comparative
479 simulations in detergent micelles and lipid bilayer have so far not been performed.
480 Among three models, model 2 is considered as the most realistic model and was
481 chosen as working model for the E-S in our study. Our simulation results on PSH

clearly showed more structural fluctuations of the protease in the micelle environment than in the membrane environment. These translated into less stable interactions with the substrate in the micelle compared to that in the bilayer, particularly of TMD6a with C83 in the active site region. In line with our mutational analysis, changing residues within the hydrophobic patch of TMD6a, which interacts with residues V50 and L52 at or near, respectively, the ε49-site of the substrate, disrupted interactions with the substrate in the MD simulations and strongly interfered with substrate cleavage in the PSH cleavage assays thus linking functional biochemical data with structural dynamics of PSH. TMD6a thus further emerges as an important structural element for substrate interaction that appears to be able to sense changes in the hydrophobic environment of the protease. The increased stability of TMD6a in POPC reflects a stabilized enzyme-substrate interaction that could likely translate into the enhanced processivity observed for the membrane environment. A more stable interaction increases the substrate residence time at the enzyme that has been shown for γ-secretase to be key for its processivity [51] and that is also supported by MD simulations of a γ-secretase–C99 complex [52]. Moreover, a closer distance of the catalytic aspartate residues was much more frequently observed for the substrate-bound PSH holo form in the POPC bilayer suggesting that the formation of an active site geometry capable of peptide bond hydrolysis is promoted in the membrane environment. Consistent with these data, we found that binding of PSH to Merck C, a biotinylated derivative of L-685,458, was increased in the POPC bilayer. As shown previously for γ-secretase, L-685,458 interacts with the same subsite pockets as C83 and occupies a position of the substrate in the active site region close to where also the ε-cleavage sites of C83 become exposed and are unfolded [29,48].

Despite the demonstration of direct binding of the L-685,458 lead structure to PSH using the Merck C affinity ligand, L-685,458 inhibited PSH much less efficiently

than γ-secretase, i.e. micromolar concentrations were needed to inhibit PSH compared to nanomolar concentrations known to inhibit γ-secretase. Likewise, and consistent with previous results [16], the related TSA inhibitor III-31C could inhibit C99 cleavage of PSH but again at micromolar concentrations. Since other non-TSA GSIs failed to inhibit PSH, only TSA inhibitors can interact with PSH and effectively inhibit the enzyme. This suggests that the binding sites for non-TSA GSIs are different or, more likely, that their interactions with PSH are too weak to inhibit the enzyme. As shown previously, the binding sites of the non-TSA GSIs Avagacestat and Semagacestat are similar to the binding site of the TSA GSI L-685,458 [29]. The non-TSA GSIs occupy the position of the β-strand of the substrate but do not protrude to the catalytic site resulting in decreased interactions with γ-secretase compared to the TSA GSI [29].

Both our experimental studies and the corresponding comparative MD simulations therefore suggest that the higher conformational flexibility of PSH in micelles causes destabilized interaction with C83 and C99 and consequently a reduced processivity. In contrast, a lipid bilayer induces a less flexible conformation of PSH that allows a more stable interaction with substrate, thereby promoting the processivity of PSH. Our data support recent findings for γ-secretase that showed differences in the processivity in micelles and a lipid raft-like membrane environment [53] and now provide an underlying molecular basis for this behavior. Similar to an artificial destabilization of the PSH/presenilin fold in detergent micelles, computational analyses suggest that FAD mutations in presenilin cause structural destabilizations [41,54,55] which are consistent with the experimentally observed impact on substrate interactions of these mutants [56,57] and their alteration of APP/Aβ E-S stabilities resulting in processivity impairments [53]. We also note that a less stable E-S in detergent micelles might account for differences in cleavage site usage and in

534 inhibition profiles for diverse C99-based substrates that were observed in previous
535 PSH assays [15,16,18].

536 Presumably, due to their non-native environment, the available structures of
537 GxGD-type proteases show catalytically inactive conformations with too distant
538 catalytic residues. The large distance of the catalytic aspartates of PSH in the
539 substrate-free apo form is also seen for γ-secretase (10.6 Å, [25]) as well as in different
540 GxGD-type aspartyl proteases like FlaK (12 Å, [58]) and seems to represent their
541 inactive form. Upon substrate interaction, this distance is decreased bringing the two
542 catalytic aspartates closer to the initial cleavage sites [26,27]. As now shown in our
543 study, a lipid bilayer environment promotes the formation of a stable active-site
544 geometry by bringing the catalytic residues, water and the substrate scissile bonds
545 into a conformation that allows proteolysis to proceed more efficiently. As a general
546 implication for intramembrane proteolysis, our data suggest that a lipid bilayer-
547 mediated stabilization of the active-site geometry might also be observable for other
548 intramembrane proteases of different catalytic types.

549 Taken together, in good correlation between experimental and simulation data,
550 our results with PSH as a model intramembrane protease highlight an important role
551 of the membrane lipid environment in providing a stabilized E-S conformation that is
552 crucial for substrate processing in intramembrane proteolysis. Our data further
553 underscore a key role of the conformational flexibility of presenilin/PSH TMD6a for
554 substrate interactions and proteolytic cleavage of presenilin-type proteases. Most
555 importantly, they provide evidence that the lipid bilayer promotes the formation of a
556 conformationally stable active site geometry, which is of general importance for an
557 efficient catalytic operation of intramembrane proteases.

558

559 **APPENDIX 1**

Protein quality control

To check for the quality of the protein preparations, WT and mutant PSH were analyzed by DLS, BN-PAGE and nanoDSF. In DLS experiments, the Z-Average (Z-Ave) value for WT and mutant PSH was below 100 nm, which indicates that the different PSH preparations were not aggregated (**Appendix 1 – figure 1A**). BN-PAGE immunoblot analysis showed a band for monomeric and dimeric PSH for all constructs but no higher molecular weight aggregate formation was observed (**Appendix 1 – figure 1B**). nanoDSF experiments showed an inflection temperature (T_i) of round about 72.5 °C for all constructs (**Appendix 1 – figure1C**) indicating that the introduction of single point mutations into PSH does not influence the thermal stability and folding of the protein.

MATERIALS AND METHODS

Key Resources Table				
Reagent type (species) or resource	**Designation**	**Source or reference**	**Identifiers**	**Additional information**
Strain, strain background (*Escherichia coli)*	$BL21(DE3)_{RIL}$	Agilent Technologies	Cat# 230245	
Recombinant DNA reagent	pQE60-C100-His_6	Edbauer et al. 2003 [21]	N/A	
Recombinant DNA reagent	pQE60-C83-His_6	This study	N/A	
Recombinant DNA reagent	pET21b-PSH	Li et al. 2013 [23]	N/A	Gift from Yigong Shi
Antibody	Anti-APP (C-terminus) Y188 (rabbit monoclonal)	Abcam	Cat# ab32136	IB (immunoblot) (1:5000)

Antibody	Anti-APP (C-terminus) 6687 (rabbit polyclonal)	Steiner et al. 2000 [8]	N/A	IP (immunoprecipitation) (1:100–1:200)
Antibody	Anti-APP (Aβ22-35) (rabbit polyclonal)	Sigma-Aldrich	Cat# A3356	IB (1:1000)
Antibody	Anti-APP (Aβ1-16) 2D8 (mouse monoclonal)	Shirotani et al. 2007 [59]	N/A	IB (3 µg/ml)
Antibody	Anti-APP (Aβ17-24) 4G8 (mouse monoclonal)	BioLegend	Cat# 800702	IB (1:500-1:2500)
Antibody	Anti-PSH (residues 192-204) 6F4 (rat monoclonal)	This study	N/A	IB (3 µg/ml), generation of antibody described further below
Antibody	Anti-Penta-His (mouse monoclonal)	Qiagen	Cat# 34660	IB (1:1000)
Chemical compound, drug	Ni-NTA Agarose	Qiagen	Cat# 30210	
Chemical compound, drug	Calbiosorb Adsorbent beads	Calbiochem	Cat# 206550	Discontinued
Chemical compound, drug	POPC	Avanti Polar Lipids	Cat# 850457P	Powder
Chemical compound, drug	Rhodamine-DHPE	Invitrogen	Cat# L1392	
Chemical compound, drug	Sephacryl S-200 HR	GE Healthcare	Cat# 17058410	

Chemical compound, drug	Streptavidin Sepharose	GE Healthcare	Cat# 17511301	
Chemical compound, drug	L-685,458	Sigma-Aldrich	Cat# 565771	InSolution γ-Secretase Inhibitor X, used in cleavage assays
Chemical compound, drug	L-685,458	Sigma-Aldrich	Cat# L1790	Powder, dissolved in DMSO and used in inhibitor affinity precipitation experiments
Chemical compound, drug	Merck C	Taros Chemicals	N/A	Biotinylated L-685,458
Chemical compound, drug	n-Dodecyl β-D-maltoside (DDM)	Millipore	Cat# 324355	
Chemical compound, drug	Protein G Sepharose	Cytiva	Cat# 17061801	
Chemical compound, drug	Protein A Sepharose	Cytiva	Cat# 17528001	
Chemical compound, drug	Tropix I-BLOCK	Invitrogen	Cat# T2015	
Chemical compound, drug	III-31C	Sigma-Aldrich	Cat# C0619	
Chemical compound, drug	DAPT	Boehringer Ingelheim Pharma KG	N/A	
Chemical compound, drug	LY411575	Karlheinz Baumann	N/A	
Chemical compound, drug	Begacestat	Karlheinz Baumann	N/A	
Chemical compound, drug	MRK-560	Karlheinz Baumann	N/A	

Commercial assay or kit	V-PLEX Plus Aβ Peptide Panel 1 (4G8) Kit	Meso Scale Discovery	Cat# K15199G	
Commercial assay or kit	NativePAGE ™ 4 to16 %, Bis-Tris, 1.0 mm, Mini Protein Gels, 10 wells	Invitrogen	Cat# BN1002BOX	
Software, algorithm	GelAnalyzer 19.1	Istvan Lazar Jr., PhD Istvan Lazar Sr., PhD, CSc	N/A	www.gelanalyzer.com
Software, algorithm	AMBER18	Case et al. 2018 [59]	N/A	
Software, algorithm	CHARMM-GUI	Jo et al 2008 [60]	N/A	
Software, algorithm	SWISS-MODEL	Waterhouse et al. 2018 [61]	N/A	
Software, algorithm	PROPKA3.1	Olsson et al. 2011 [62] Sondergaard et al. 2011 [63]	N/A	
Software, algorithm	DSSP	Kabsch & Sanders 1983 [64] Touw et al. 2015 [65]	N/A	

Monoclonal antibody generation

Monoclonal antibody 6F4 (IgG2b/k) to PSH was raised in Wistar rat against amino acid residues 192-204 (KRADYSFRKEGLN) of PSH from *Methanoculleus marisnigri.*

PSH constructs

All constructs are based on the PSH expression construct in pET-21b used for structure determination [23]. PSH point mutations and deletion were generated using

site-directed mutagenesis. DNA sequencing of the newly generated plasmid confirmed successful mutagenesis.

PSH expression and purification

Expression and purification of WT and mutant PSH was adopted from the published protocol [23]. In brief, *E. coli* BL21(DE3) cells transformed with the pET-21b vector harboring an N-terminal 8x His-tagged PSH were grown in LB medium to an optical density of 1.5 and expression was induced with 0.2 mM isopropyl β-D-1-thiogalactopyranoside (IPTG). PSH was expressed at 22 °C overnight and harvested cells were resuspended in resuspension buffer (25 mM Tris-HCl, pH 8.0, 150 mM NaCl). Cells were lysed by sonication; cell debris was removed by centrifugation and membranes were collected by ultracentrifugation at 150,000 x *g* for 1 h. Membranes were solubilized in resuspension buffer containing 2% DDM by rocking at 4 °C for 2 h. After ultracentrifugation at 150,000 x *g* for 30 min, the supernatant was incubated with Ni-NTA agarose beads (Qiagen) for 2 h at room temperature. Beads were then washed with resuspension buffer containing 20 mM imidazole and 0.6% (w/v) DDM. PSH was eluted with resuspension buffer containing 250 mM imidazole and 0.6% (w/v) DDM. Correct folding of WT and mutant PSH was confirmed by dynamic light scattering (DLS, Malvern Instruments High Performance Particle Sizer) (**Appendix 1 – figure 1A),** Blue Native (BN)-PAGE (**Appendix 1 – figure 1B)** and nano differential scanning fluorimetry (nanoDSF, NanoTemper Tycho) (**Appendix 1 – figure 1C).** For DLS, protein samples (25 µM) were analyzed in a Hellma Analytics High Precision Cell. For BN-PAGE, samples were prepared as described [66] and separated using a Novex NativePAGE 4-16% Bis-Tris gel. Following electrophoresis, the gel was prepared for blotting as described [67] and WT and mutant PSH were subjected to immunoblot analysis with antibody 6F4. For nanoDSF, protein samples (25 µM)

606 were loaded into NanoTemper Tycho NT.6 capillaries, unfolding profiles of WT and
607 mutant PSH were recorded, and the inflection temperatures (T_i) were obtained by
608 automated data analysis.
609
610 **PSH reconstitution in POPC vesicles**
611 PSH reconstitution into POPC SUVs was based on the reconstitution of γ-secretase
612 into SUVs [36]. SUVs were prepared in a low citrate buffer (5 mM sodium citrate, 3.5%
613 glycerol, pH 6.4) and diluted 2.5 times with buffer (5 mM sodium citrate, 3.5%
614 glycerol, 30 mM DTT, pH 6.4). One volume of purified PSH and four volumes of the
615 vesicle preparation were mixed in the presence of an excess of Calbiosorb adsorbent
616 beads (Calbiochem) and incubated at 4 °C overnight to allow the formation of
617 proteoliposomes.
618
619 **Validation of PSH reconstitution into POPC SUVs**
620 To validate the incorporation of PSH into POPC vesicles, PSH was reconstituted into
621 POPC vesicles containing the fluorescent marker lipid rhodamine-DHPE. These
622 vesicles were then subjected to a small gel filtration column packed with Sephacryl S-
623 200 HR to separate vesicles and free PSH. The vesicle content of each fraction was
624 analyzed by measuring fluorescence (λ_{ex} 530 nm, λ_{em} 590 nm) with Fluoroscan Asket
625 FI (Labsystems) and the presence of PSH in the fractions was analyzed by
626 immunoblotting with antibody 6F4.
627
628 **APP substrate constructs**
629 Recombinant APP substrate C100-His_6 was described before [21]. The corresponding
630 C83-His_6 (containing an N-terminal methionine) was generated by PCR and cloned
631 into pQE60.

632

633 **Expression and purification of APP-based substrates**

634 C100-His_6 and C83-His_6 were expressed in *E. coli* BL21$(DE3)_{RIL}$ cells after induction
635 with IPTG at 37 °C for 4 h. Cell pellets were resuspended in TE buffer (20 mM Tris
636 (pH 7.5), 1 mM EDTA), sonified and inclusion bodies were collected by centrifugation.
637 Inclusion bodies were lysed overnight at 4 °C in 20 mM Tris (pH 8.5), 6 M urea,1 mM
638 $CaCl_2$, 100 mM NaCl, 1% (w/v) SDS and 1% (v/v) Triton X-100 by rotation. The
639 lysate was diluted 1:5 with 20 mM Tris (pH 7.5) and 150 mM NaCl and then
640 incubated with Ni-NTA agarose for 2 h at room temperature. Ni-NTA beads were
641 washed extensively with TX-wash buffer (50 mM Tris (pH 8.5), 300 mM NaCl, 1%
642 (v/v) Triton X-100), SDS-wash buffer (50 mM Tris (pH 8.5), 300 mM NaCl, 0.2% (w/v)
643 SDS) and imidazole wash buffer (50 mM Tris (pH 8.5), 300 mM NaCl, 0.2% (w/v)
644 SDS, 20 mM imidazole) before the elution of bound protein with elution buffer (50 mM
645 Tris (pH 8.5), 300 mM NaCl, 0.2% (w/v) SDS, 150 mM imidazole).

646

647 **PSH *in vitro* assay**

648 The *in vitro* assays using recombinant APP substrates C100-His_6 and C83-His_6 was
649 performed with either DDM-solubilized PSH or reconstituted PSH. To test PSH
650 activity over a range of different pH values, the *in vitro* assay was performed in the
651 presence of a master buffer (20 mM Bicine, 20 mM HEPES, 20 mM MES) adjusted to
652 different pH values (pH 5.5 to 9.0). 1 - 2 μM PSH was incubated with 0.5 μM
653 substrate overnight at 37 °C. The final DDM concentration was 0.02% for the assays
654 in DDM micelles. For the assays with PSH reconstituted in POPC vesicles a small
655 amount of DDM was added just below the critical micelle concentration (CMC) of
656 0.0087%. As for γ-secretase, detergent addition below the CMC is necessary to
657 achieve enzyme activity after reconstitution [36]. Generated AICD, Aβ and p3 were

analyzed by immunoblotting and in addition, Aβ and AICD species were determined by MALDI-TOF mass spectrometry (MS) analysis as described previously [67-69]. In brief, samples were diluted with IP-MS buffer (10 mM Tris (pH 8.0), 140 mM NaCl, 0.5 mM EDTA, 0.1% n-octyl-glucopyranoside) and immunoprecipitated for 16 h at 4 °C with antibody 4G8 and protein G Sepharose for Aβ species or with antibody 6687 and protein A Sepharose for AICD species.

Electrochemiluminescence immunoassay (ECL-IA)

Aβ and p3 species from PSH *in vitro* assays were analyzed with the V-PLEX Plus Aβ Peptide Panel 1 (4G8) Kit (Meso Scale Discovery, K15199G) using SULFO-tagged anti-Aβ antibody (4G8) in a 1:50 dilution. Samples were centrifuged for 30 min at 21,000 x *g* and then diluted 1:25 to reach a sample concentration in the linear detection range. The ECL-IA was performed following the manufacturer's protocol.

Inhibitor affinity precipitations of PSH

Streptavidin Sepharose beads (GE Healthcare) were washed three times with PBS and then blocked overnight with 1% I-Block in PBS at 4 °C and additionally for 30 min at room temperature. PSH in DDM micelles or in POPC vesicles was diluted with MES-buffer (50 mM MES pH 6.0, 500 mM NaCl, 5 mM $MgCl_2$, 1x PI mix complete (Roche)) to 1 - 2 µM PSH. To mimic the cleavage assay condition, a small amount of DDM was added just below the CMC of DDM (0.0087%) to the POPC reconstituted PSH. The diluted PSH solution was precleared with streptavidin beads for 30 min at 4 °C. To capture PSH, the precleared solution was incubated with 20 µM L-685,458-based biotinylated TSA inhibitor Merck C [42] (Taros Chemicals) in the presence of

streptavidin beads for 2 h at room temperature. To analyze non-specific binding, Merck C was omitted or a 100-fold molar excess of the parental compound L-685,458 was added. To quantify Merck C GSI binding to PSH, the chemiluminescence signal of the respective immunoblots were quantified using the LAS-4000 image reader (Fujifilm Life Science) and GelAnalyzer 19.1 software (www.gelanalyzer.com). Specific binding was calculated as the difference between the binding of PSH and the binding of PSH in presence of the competitor L-685,458 after subtraction of unspecific PSH binding to the beads.

Molecular dynamics simulations

The available crystal structures of PSH, PDB 4HYG [23] and PDB 4Y6K [16] include several amino acid substitutions compared to the WT PSH sequence and in addition, several important loop segments are missing. In both crystals, the enzyme forms a tetramer that may also stabilize a structure different from the solution and substrate-bound conformation. Under the assumption that a substrate is bound to PSH in an analogous fashion as in the PS1 homolog, we used the option to generate a comparative model structure using the C83 substrate-bound γ-secretase structure (PDB 6IYC) [26] as a template. Three models were generated using the SWISS online server [61] and the program MODELLER [70] with a same sequence alignment strategy (**Figure 4 – figure supplement 2**) but different homology protocols. Model 1 was built by taking only PDB 6IYC as the template as generated by the SWISS online server (**Table 1**). Model 2 was generated by using residues ranging from L7 to D162 and D220 to L292 from chain B of PDB 4HYG and model 1 as templates with the MODELLER multi-template method (**Table 1**). Model 3 was built by taking all residues resolved in chain B of PDB 4HYG and model 1 with the MODELLER multi-template method (**Table 1**). Similar to the PS1 template structure, the final holo PSH

structure is composed of two fragments with an N-terminal fragment from L7-R193 and a C-terminal fragment from E210 to A293. The generated holo-state PSH structures were then embedded in two different environments: micelle capsules consisting of 150 DDM molecules and a membrane bilayer with 302 POPC molecules. An additional, larger micelle capsule system of model 2 was constructed with 50% more, namely 225, DDM, molecules. Lysine mutations M172K, I173K, L175K and A176K were constructed based on model 2 with RMSD (WT vs mutant) < 0.1 Å, and embedded in a membrane bilayer system with 302 POPC molecules using the CHARMM-GUI online server. All 11 systems were prepared and solvated in explicit TIP3P water [71] at a salt concentration of 0.15 M KCl using the CHARMM-GUI online server. [72,73].

The interaction of proteins, lipid and micelles is described by the charmm36m force field [74]. Each system was simulated using the AMBER18 pmemd GPU accelerated version [59] in combination with a Berendsen barostat (1 bar) and a Langevin thermostat (303.15 K). The hydrogen mass repartitioning method was used allowing a time step of 4 fs. Three simulations with 600 ns each were performed for each system, in total 33 NPT trajectories were generated for further analysis. Non-bonded cutoff was set to 12 Å with a force-based switching distance of 10 Å. D220 was selected to be protonated while D162 was unprotonated according to the pK_a prediction on the existing PSH and PS1 structures by PROPKA3.1 [62,63] (**Table 2**).

The lipid tail order parameter S_{CH} was computed in model 2 in DDM and POPC environments to show the orientation and the ordering of the concerning CH vector [75,76] with respect to the protein principle axis, which was aligned to the lipid normal in the POPC environment. In addition, the area per lipid was computed in model 2 on both leaflets to verify the reliability of our POPC lipid model.

RMSF of PSH and C83 curves were calculated by taking the last 200 ns with the time-average PSH structure of each simulation as the reference and only taking the backbone atoms for the calculation. Secondary structure of PSH TMD6a was calculated using the DSSP method [64,65].

ACKNOWLEDGEMENTS

We thank Yigong Shi for the PSH expression plasmid, Karlheinz Baumann for GSIs and Gabriele Basset, Frits Kamp and Alice Sülzen for technical assistance as well as Shibojyoti Lahiri, Ignasi Forné and Axel Imhof from the Protein Analysis Unit of the Biomedical Center Munich (BMC) and Michaela Smolle from the Biophysics Core Facility of the BMC for access to their instruments, helpful discussions and advice.

COMPETING INTERESTS

The authors declare no competing interests.

FIGURE LEGENDS

Figure 1. Cleavage of APP C99 by PSH.

(A) Schematic illustration of APP C99 cleavage by PSH. PSH cleaves C99 and releases an AICD fragment and Aβ peptides. The epitope of the PSH specific antibody 6F4 in the loop between TMD6 and TMD7 is indicated.

(B) Analysis of PSH activity in DDM micelles after incubation with C100-His_6 substrate overnight at 37 °C by immunoblotting for AICD (Y188) and Aβ (2D8). Specificity of substrate cleavage by PSH in the assay was controlled by sample incubation at 4 °C or 37 °C in presence of the GSI L-685,458 (20 μM). Immunoblotting of PSH (6F4) was performed to control for PSH levels.

(C) Aliquot of samples from (B) separated by Tris-Bicine urea SDS-PAGE for identifying Aβ species produced by PSH in DDM micelles and analysis by immunoblotting (2D8). In (B) and (C), representative immunoblots from 3 to 6 independent biological replicates (i.e. independent protease preparations) are shown. **(D)** Representative MALDI-TOF MS spectrum of Aβ profile generated by PSH in DDM micelles from 4 independent biological replicates. The intensity of the highest peak was set to 100%. A GSI control is shown in **Figure 1 – figure supplement 1** and observed masses for identified Aβ species are shown in **Figure 1 – source data 1.**

Figure 2. Comparison of PSH cleavage activity and processivity in DDM micelles and POPC bilayer.

(A) Analysis of PSH activity in DDM micelles and POPC vesicles after incubation with C100-His_6 substrate at 37 °C overnight by immunoblotting for AICD (Y188) and Aβ (2D8). Immunoblotting of PSH (6F4) was performed to control for PSH levels.

(B) Separation of Aβ species produced by PSH in DDM micelles and POPC vesicles by Tris-Bicine urea SDS-PAGE and analysis by immunoblotting for Aβ (2D8). In (A) and (B), representative immunoblots from 6 independent biological replicates are shown. Confirmation of PSH reconstitution in POPC SUVs is shown in **Figure 2 – figure supplement 1.**

(C, D) MALDI-TOF MS analysis of Aβ (C) and AICD (D) species generated by PSH in DDM micelles and POPC vesicles at pH 7.0. Representative mass spectra from 4 independent biological replicates are shown. The intensity of the highest peak was set to 100%. GSI controls are shown in **Figure 2 – figure supplement 2** and

observed masses for identified Aβ and AICD species are shown in **Figure 2 – source data 1.**

Figure 3. Cleavage of APP C83 by PSH.

(A) Analysis of PSH activity in DDM and POPC environment after incubation with C83-His_6 and C100-His_6 substrates at 37 °C and pH 7.0 by immunoblotting for AICD (penta-His) and p3 (Aβ (22-35)). Immunoblotting of PSH (6F4) was performed to control for PSH levels.

(B, C) p3-40/p3-42 ratio (B) and Aβ40/Aβ42 ratio (C) from PSH activity assays in DDM (red) and POPC (blue) environment analyzed by ECL-IA. Quantitative data are represented as mean ± standard deviation (SD) (n = 3 biological replicates). Source data are shown in **Figure 3 – source data 1.**

Figure 4. PSH homology model.

(A) Alignment of the modeled holo form (model 2) of PSH (blue) with APP C83 substrate (orange) and the crystal structure of PSH (PDB 4HYG) in the apo form (green) in side view (left panel) and top view (right panel). An overlay of all three models and their RMSD values are provided in **Figure 4 – figure supplement 1A and B**.

(B) Schematic representation of the hydrogen bonds formed between β3 of the substrate (orange), β2, and Q272, respectively, of PSH (blue).

(C) Interaction of TMD3 and TMD6a in the C83-bound PSH model through residues R70 and E181.

(D) Interaction of TMD3 and TMD6a through residues Y159 and R278 in the C83-bound γ-secretase cryo-EM structure (PDB 6IYC).

(E) Analysis of WT and mutant PSH activity in DDM and POPC environment after incubation with C100-His_6 substrate at 37 °C overnight by immunoblotting for AICD (Y188) and Aβ (2D8). Immunoblotting of PSH (6F4) was performed to control for PSH levels. The asterisks mark two substrate degradation bands, which are independent of PSH cleavage.

Figure 5. MD simulations of holo PSH forms in DDM micelle or POPC bilayer.

(A) PSH with bound C83 substrate (model 2) embedded in a DDM micelle environment (upper panel) and a POPC bilayer (lower panel).

(B) The average number of H-bonds formed between the β3-strand of C83 and the β2-strand of PSH. Each data point stands for the average value throughout one trajectory and the error bars represent the SD of the mean of three data points.

(C) The backbone RMSF of C83 of different models in DDM (red) and POPC (blue) environments averaged over three trajectories. The shaded areas represent the SD of the mean.

(D) Water accessibility along the substrate TMD residues extracted from the simulations of the holo PSH in DDM (red) and POPC (blue) environments (water accessibility for a residue is obtained as the mean number of water molecules within 5 Å of any atom of the residue). The red arrows indicate the position of the two ε-cleavage sites. The error bars represent the SD of the mean (n = 3 trajectories).

(E) The backbone RMSF of PSH of different models in DDM (red) and POPC (blue), environments averaged over three trajectories (note that residues 194-209 are not included in our PSH models). The gray boxes highlight TMD6a and the shaded areas represent the SD of the mean. Enlarged views on backbone RMSF of residues K170 to P185 (including TMD6a) are shown in **Figure 5 – figure supplement 1B**.

Figure 6. Destabilization of PSH TMD6a in a DDM micelle.

(A) Hydrophobic interactions between PSH regions and the C83 substrate. The right panel shows an enlarged view of the interaction of a hydrophobic patch (gray surface) of TMD6a with V50 and L52 of the substrate in the POPC bilayer.

(B, C) Snapshots of the DDM insertion between TMD2 and TMD6 in the first (B) and second (C) run of the simulations in DDM environment at 400 ns. The right panels show an enlarged view of the unspecific hydrogen bonding interactions between the DDM molecule and the TMD6a amino acid backbones.

(D) Snapshot of the DDM insertion between TMD3 and TMD4 of the simulation in DDM environment at 430 ns. The right panel shows an enlarged view of the unspecific hydrogen bonding interactions between the DDM molecule and the amino acid backbones of the residues immediately C-terminal of TMD6a.

Figure 7. Impact of PSH TMD6a mutations on PSH structural dynamics and activity.

(A) RMSD of the WT (blue) and the mutated systems M172K (violet), I173K (green), L175K (gray), and A176K (orange) in the POPC bilayer environment. The solid, dashed, and dotted lines represent three different simulations with random initial velocities. The black dashed line indicates an RMSD of 4 Å.

(B) The backbone RMSF of C83 of WT PSH and different TMD6a lysine mutants in POPC environment averaged over three trajectories. The shaded areas represent the SD of the mean.

(C) Water accessibility along the substrate TMD residues extracted from the simulations of the four lysine-mutant holo-form PSH systems in the POPC bilayer environments (water accessibility for a residue is obtained as the mean number of

water molecules within 5 Å of any atom of the residue). The red arrows indicate the position the two ε-cleavage sites. The error bars represent the SD of the mean (n = 3 trajectories).

(D) The average H-bond formed between the β3-strand at the C-terminus of C83 and the β2-strand of WT and lysine-mutated PSH. Each data point stands for the average value throughout one trajectory and the error bars represent the SD of the mean of three data points.

(E) The backbone RMSF of WT (blue) and M172K (violet), I173K (green), L175K (gray), and A176K (orange) mutated PSH in POPC. The box highlights TMD6a and the shaded areas represent the SD of the mean (n = 3 trajectories). Larger RMSF of the A176K mutant observed in residues 235-243 correspond to a folding-unfolding event in the mobile loop between TMD7 and TMD8 in the third trajectory (see **Figure 7 – source data 11**).

(F) Analysis of WT and lysine-mutant PSH activity in DDM and POPC environment after incubation with C100-His_6 substrate at 37 °C overnight by immunoblotting for AICD (Y188) and Aβ (2D8). Immunoblotting of PSH (6F4) was performed to control for PSH levels. The asterisks marks substrate degradation bands, which are independent of PSH cleavage.

Figure 8. Stabilization of the PSH active site geometry in a POPC bilayer.

(A) Histograms of the Cγ-Cγ distances between the D162 and D220 of PSH measured in DDM micelle (red) and POPC bilayer (blue) environments. The dashed line indicates the distance of 7 Å. The measured distances over time are shown in **Figure 8 – figure supplement 1C**.

(B) Snapshot of the catalytic cavity in DDM (left panel) and POPC (right panel) environment. The Cγ-Cγ distance between the two catalytic aspartates D162 and

889 D220 is larger in DDM micelles and more water molecules enter the catalytic cavity
890 between D162 and the substrate. Detailed geometries of these two active site
891 conformations are depicted in **Figure 8 – figure supplement figure 2**.
892 **(C)** Immunoblot analysis of TSA-inhibitor binding to PSH in DDM micelles or POPC
893 vesicles. PSH was affinity-precipitated by Merck C (a biotinylated derivative of L-
894 685,458; 20 μM). To control for background binding and binding specificity, the
895 affinity precipitation was assessed in the absence of Merck C as well as in the
896 presence of excess amounts of the parental compound L-685,458 (2 mM) as
897 competitor. The input represents 2.5% of the total sample used for the affinity
898 precipitation. A representative immunoblot from 4 independent biological replicates
899 is shown.
900 **(D)** Quantitation of PSH binding by Merck C. Specific binding was defined as
901 difference of PSH signals in the absence or presence of L-685,458 after additional
902 subtraction of unspecific background binding signals. Quantitative data are
903 represented as mean ± SD (n = 4 biological replicates). The source data are shown
904 in **Figure 8 – source data 1.**
905 **(E, F)** Inhibition assay of PSH in DDM micelles and POPC vesicles with increasing
906 concentrations of L-685,458 (E) or Merck C (F), respectively. PSH activity was
907 analyzed by immunoblotting for AICD (Y188) and Aβ (2D8) following incubation with
908 C100-His_6 substrate at 37 °C overnight. Representative immunoblots from 3
909 independent biological replicates are shown. The asterisks mark two substrate
910 degradation bands, which are independent of PSH cleavage.
911 **(G)** Inhibition assay of PSH reconstituted in POPC vesicles in the presence of 20 μM
912 TSA and non-TSA γ-secretase inhibitors. PSH activity was analyzed by
913 immunoblotting for AICD (Y188) and Aβ (2D8) following incubation with C100-His_6

substrate at 37 °C overnight. Representative immunoblots from 3 independent biological replicates are shown.

TABLES

Table 1. Templates used for model building of PSH in complex with C83. Residues of PSH used for model building are indicated.

	Template		
	6IYC (PS1, C83)	**4HYG (Chain B)**	**Model 1**
Model 1	*	–	–
Model 2	–	L7-D162, D220-L292	complete
Model 3	–	L7-A176, E210-A293	complete

* PSH residues L7-R193 and E210-A293 were modeled based on the template.

Table 2. pK_a predictions as calculated by PROPKA3.1 for published PSH and γ-secretase structures. pKa values of the catalytic aspartate residue which is most likely protonated are indicated in red.

PDB ID	Enyzme	Ligand	pKa (D162, D220)
4HYG	PSH	None	5.04, 6.62
4Y6K	PSH	III-31-C	5.63, 7.52

PDB ID	Enyzme	Ligand	pKa (D257, D385)
4UIS	PS1	None	3.18, 6.16
5A63	PS1	None	4.42, 6.16

5FN5	PS1	None	4.98, 3.63
5FN4	PS1	Unknown helix	4.70, 4.71
5FN3	PS1	Unknwon helix	4.90, 7.13
5FN2	PS1	DAPT	5.13, 9.93
6IYC	PS1	C83	6.39, X*
6IDF	PS1	Notch1	6.21, X*
6LR4	PS1	Semagacestat	6.12, 7.94
6LQG	PS1	Avagacestat	6.08, 7.22
7V9I	PS1	L-685,458	7.11, 8.90
7D8X	PS1	L-685,458 & E2012	7.01, 8.69

* For structure determination D385 was mutated to alanine and therefore no pKa value is given.

FIGURE SUPPLEMENTS

Figure 1 – figure supplement 1. MS specificity control for Aβ cleavage products generated from APP C99 by PSH.

Representative MALDI-TOF MS spectrum of PSH cleavage assay in DDM micelles in the presence of L-685,458 from 4 independent biological replicates. The intensity of the highest peak was set to 100%.

Figure 2 – figure supplement 1. Reconstitution of PSH in POPC vesicles.

(A) Fluorometric analysis of gel filtration fractions of PSH-containing POPC vesicles with rhodamine-DHPE as fluorescent marker lipid. A representative graph from 3 independent biological replicates is shown.

(B) Analysis of gel filtration fractions by immunoblotting for PSH (6F4). A representative immunoblot from 3 independent biological replicates is shown.

Figure 2 – figure supplement 2. MS specificity controls for Aβ and AICD cleavage products generated from APP C99 by PSH.

(A, B) MALDI-TOF MS analysis of Aβ (A) and AICD (B) species from PSH cleavage assays in DDM micelles and POPC vesicles in the presence of L-685-458 at pH 7.0. Representative mass spectra from 4 independent biological replicates are shown. The intensity of the highest peak was set to 100%.

Figure 4 – figure supplement 1. Comparison of the three different homology models.

(A) Alignment of the three modeled holo forms of PSH in side view (left panel) and top view (right panel).

(B) RMSD values between the available crystal structures (PDB 4HYG and 4Y6K) and the three different PSH models.

Figure 4 – figure supplement 2. Alignment of PS1 and PSH used for homology modelling based on the TMD annotations of the available cryo-EM or crystal structures, respectively (PDB 6IYC for PS1 and PDB 4HYG for PSH). Active site motifs including the catalytic aspartate residues (red) are highlighted in bold. The β2-strands of γ-secretase and PSH are indicated as orange arrows and residues that were mutated in this study are highlighted in violet.

Figure 5 – figure supplement 1. Homology modelling of the holo form PSH in complex with C83 in DDM and POPC environments.

(A) The backbone RMSD of PSH of different models in DDM (red) and POPC (blue) averaged over three trajectories. The black dashed line indicates an RMSD of 4 Å.

(B) Enlarged representation of backbone RMSF of residues K170 to P185 (including TMD6a (orange)) of different models in DDM (red) and POPC (blue) environments

965 averaged over three trajectories. The shaded areas represent the SD of the mean
966 and the black dashed lines indicate an RMSD of 1 Å.
967
968 **Figure 5 – figure supplement 2.** Secondary structure of PSH TMD6a and
969 surrounding residues over simulation time.
970 **(A-C)** Secondary structure of PSH TMD6a (orange) and surrounding residues of
971 model 1 (A), model 2 (B) and model 3 (C) in DDM micelle (top) and POPC bilayer
972 (bottom) environments over the simulation time calculated using DSSP algorithm. As
973 indicated, 3 simulations were performed in both environments for each model.
974
975 **Figure 5 – figure supplement 3.** Comparison of model 2 and 3.
976 **(A)** Structural comparison of model 2 (blue) and 3 (gray). TMD6a is spatially closer to
977 the C83 substrate in model 2.
978 **(B)** Comparison of the backbone RMSFs of PSH model 2 (blue) and 3 (gray) in
979 POPC bilayer averaged over three trajectories. The gray box highlights TMD6a and
980 shaded areas represent the SD of the mean. An enlarged view on backbone RMSF
981 of residues K170 to P185 (including TMD6a) is shown in (C).
982 **(C)** Enlarged representation of backbone RMSF of residues K170 to P185 (including
983 TMD6a (orange)) in POPC environment for model 2 (blue) and model 3 (gray)
984 averaged over three trajectories. The shaded areas represent the SD of the mean.
985 Data in (B) and (C) are taken from **Figure 5E** and **Figure 5 – figure supplement 1B**
986 respectively**,** and are used here as an overlay to allow a direct comparison of model 2
987 and 3 in POPC bilayer.
988
989 **Figure 6 – figure supplement 1.** Hydrophobic interactions of PS1 TMD6a in
990 substrate-bound and GSI-bound γ-secretases.

(A, B) Interactions between TMD6a of PS1 and substrate residues near the scissile bond(s) in the C83-bound (A) and Notch1 (N100)-bound (B) γ-secretase cryo-EM structures (PDB 6IYC and PDB 6IDF, respectively). The van der Waals radii of TMD6a and directly surrounding residues (R268 to R278) of PS1 are shown by the gray surface.

(C, D) Interactions between TMD6a of PS1 and GSI in the Semagacestat-bound (C) and L-685,458 bound (D) γ-secretase cryo-EM structures (PDB 6LR4 and PDB 7C9I, respectively). The van der Waals radii of TMD6a and directly surrounding residues (R268 to R278) of PS1 are shown by the gray surface.

Figure 6 – figure supplement 2. Biophysical properties of DDM and POPC.

(A) Structures of DDM and POPC.

(B) Calculated lipid order parameters S_{CH} of the acyl chains of DDM (red) and POPC (sn-1 blue, sn-2 black). Data are represented as mean ± SD (n = 3 trajectories).

(C) Area per lipid of POPC molecules averaged for every 30 ns in model 2.

Figure 6 – figure supplement 3. MD simulations in different DDM micelles.

(A) PSH with bound C83 substrate embedded in a DDM micelle environment (225 DDM molecules).

(B) Calculated lipid order parameters S_{CH} of the acyl chains of DDM in small (red, 150 molecules) and large (olive, 225 molecules) micelles. Data are represented as mean ± SD (n = 3 trajectories).

(C) The average number of H-bonds formed between the β3-strand of C83 and the β2-strand of PSH in DDM micelles composed of 150 molecules (red) and 225 molecules (olive). Each data point stands for the average value throughout one trajectory and the error bars represent the SD of the mean of the three data points.

(D) The backbone RMSF of C83 in DDM micelles composed of 150 molecules (red) and 225 molecules (olive) averaged over three trajectories. The shaded areas represent the SD of the mean.

(E) Water accessibility along the substrate TMD residues extracted from the simulations in DDM micelles composed of 150 molecules (red) or 225 molecules (olive) (water accessibility for a residue is obtained as the mean number of water molecules within 5 Å of any atom of the residue). Red arrows indicate the position of the two ε-cleavage sites. The error bars represent the SD of the mean (n = 3 trajectories).

(F) The backbone RMSF of PSH in DDM micelles composed of 150 molecules (red) and 225 molecules (olive) averaged over three trajectories. The shaded areas represent the SD of the mean. An enlarged view on backbone RMSF of residues K170 to P185 (including TMD6a) is shown in (G).

(G) Enlarged representation of backbone RMSF of residues K170 to P185 (including TMD6a (orange)) in small (red) and large (olive) DDM micelles averaged over three trajectories. The shaded areas represent the SD of the mean.

(H) Orientation of DDM molecules around HL1 and TMD6a in DDM micelles composed of 150 molecules (left, red) and 225 molecules (right, olive).

Figure 7 – figure supplement 1. Secondary structure of lysine-mutant PSH TMD6a and surrounding residues over simulation time.

Secondary structure of PSH TMD6a (orange) and surrounding residues bearing lysine mutants in POPC bilayer environments over simulation time calculated using DSSP.

Figure 8 – figure supplement 1. Cγ-Cγ distances in PSH homology model.

(A) The average Cγ-Cγ distances between D162 and D220 of PSH. Each data point stands for the average value throughout one trajectory with the error bar showing the SD of the three independent trajectories.

(B) Frequency of the catalysis-compatible Cγ-Cγ distance (below 7 Å) in DDM and POPC environments.

(C) Cγ-Cγ distance measured in DDM (red) and POPC (blue) environments throughout different trajectories (solid, dashed, and dotted lines).

Figure 8 – figure supplement 2. Detailed geometry of the E-S catalytic site.

Detail geometries and distances for the atoms between D162, D220 and C83 L49 at a Cγ-Cγ distance of 8.2 Å in DDM micelles (A) and 6.8 Å in POPC bilayer (B).

Figure 8 – figure supplement 3. Chemical structures of GSIs.

(A, B) Structures of TSA GSIs L-685,458 (A) and III-31C (B).

(C-F) Structures of non-TSA GSIs DAPT (C), LY411575 (D), Begacestat (E) and MRK-560 (F).

APPENDIX FIGURE

Appendix 1 – figure 1. Quality control of WT and mutant PSH.

(A) Analysis of protein aggregation of WT and mutant PSH by DLS.

(B) Analysis of protein aggregation of WT and mutant PSH by BN- PAGE followed by immunoblotting for PSH (6F4).

(C) Analysis of protein misfolding of WT and mutant PSH by nanoDSF.

RICH MEDIA FILES

Video 1, 2. Detergent-enzyme interaction in the DDM environment.

600 ns trajectories of PSH (red) in complex with C83 (orange) and nearby DDM molecules. A DDM molecule enters into the gap between TMD2 and TMD6 (Video1) or TMD3 and TMD4 (Video 2). TMD6a switches between a helical and a loop conformation with the interference of the disordered DDM molecule.

Video 3. Lipid-enzyme interaction in the POPC environment.

600 ns trajectory of PSH (blue) in complex with C83 (orange) and nearby POPC molecules. POPC molecules. POPC molecules do not enter between TMD gaps and TMD6a remains a stable helix throughout the whole trajectory.

SOURCE DATA

Figure 1 – Source data 1. Immunoblot images (raw and annotated) of cleavage assay (Source data for **Figure 1B, C**).

Figure 1 – Source data 2.

Calculated and observed masses for Aβ species in MALDI-TOF mass spectrometry (Source data for **Figure 1D**).

Figure 2 – Source data 1. Immunoblot images (raw and annotated) of cleavage assays (Source data for **Figure 2A, B**).

Figure 2 – Source data 2. Calculated and observed masses for Aβ, and AICD species in MALDI-TOF mass spectrometry (Source data for **Figure 2C, D**). The differences between calculated and observed masses for AICD species arise from different adducts as specified in the respective tables. The GSI controls in **Figure 2 – figure supplement 2B** show that the observed peaks are specific for AICD species derived from PSH cleavage.

Figure 2 – Figure supplement 1 – Source data 1. Raw values of measured fluorescence intensity (Source data for **Figure 2 – Figure supplement 1A**).

Figure 2 – Figure supplement 1 – Source data 2. Immunoblot images (raw and annotated) of PSH reconstitution (Source data for **Figure 2 – Figure supplement 1B**).

Figure 3 – Source data 1. Immunoblot images (raw and annotated) of cleavage assays (Source data for **Figure 3A**).

Figure 3 – Source data 2. Raw values of p3 and Aβ concentrations measured in the ECL-IA and calculated p3-40/p3-42 and Aβ40/Aβ42 ratios (Source data for **Figure 3B, C**).

Figure 4 – Source data 1. Immunoblot images (raw and annotated) of cleavage assays (Source data for **Figure 4E**).

Figure 5 – Source data 1. Raw values of simulation data analysis (Source data for **Figure 5B-E**).

Figure 5 – Figure Supplement 1 – Source data 1. Raw values of simulation data analysis (Source data for **Figure 5 – Figure Supplement 1A, B**).

Figure 5 – Figure Supplement 3 – Source data 1. Raw values of simulation data analysis (Source data for **Figure 5 – Figure Supplement 3B, C**).

Figure 6 – Figure Supplement 2 – Source data 1. Raw values of simulation data analysis (Source data for **Figure 6 – Figure Supplement 2B, C**).

Figure 6 – Figure Supplement 3 – Source data 1. Raw values of simulation data analysis (Source data for **Figure 6 – Figure Supplement 3B-G**).

Figure 7 – Source data 1. Raw values of simulation data analysis (Source data for **Figure 7A-E**).

Figure 7 – Source data 2. Immunoblot images (raw and annotated) of cleavage assays (Source data for **Figure 7F**).

Figure 8 –Source data 1. Raw values of simulation data analysis (Source data for **Figure 8A** and **Figure 8 – Figure Supplement 1A-C**).

Figure 8 – Source data 2. Immunoblot images (raw and annotated) of inhibitor precipitation assay and cleavage assays (Source data for **Figure 8C, E-G**).

Figure 8 – Source data 3. Raw values of immunoblot quantitation (Source data for **Figure 8D**).

REFERENCES

1 Erez, E., Fass, D. & Bibi, E. How intramembrane proteases bury hydrolytic reactions in the membrane. *Nature* **459**, 371-378 (2009).

2 Beard, H. A., Barniol-Xicota, M., Yang, J. & Verhelst, S. H. L. Discovery of cellular roles of intramembrane proteases. *ACS Chem. Biol.* **14**, 2372-2388 (2019).

3 Steiner, H., Tagami, S., Fukumori, A. & Okochi, M. Making the final cut: pathogenic amyloid-β peptide generation by γ-secretase. *Cell Stress* **2**, 292-310 (2018).

4 Selkoe, D. J. & Hardy, J. The amyloid hypothesis of Alzheimer's disease at 25 years. *EMBO Mol. Med.* **8**, 595-608 (2016).

5 Yang, G., Zhou, R. & Shi, Y. Cryo-EM structures of human γ-secretase. *Curr. Opin. Struct. Biol.* **46**, 55-64 (2017).

6 Wolfe, M. S., Xia, W., Ostaszewski, B. L., Diehl, T. S., Kimberly, W. T. & Selkoe, D. J. Two transmembrane aspartates in presenilin-1 required for presenilin endoproteolysis and γ-secretase activity. *Nature* **398**, 513-517 (1999).

7 Li, Y. M., Xu, M., Lai, M. T., Huang, Q., Castro, J. L., DiMuzio-Mower, J., Harrison, T., Lellis, C., Nadin, A., Neduvelli, J. G., Register, R. B., Sardana, M. K., Shearman, M. S., Smith, A. L., Shi, X. P., Yin, K. C., Shafer, J. A. & Gardell, S. J. Photoactivated γ-secretase inhibitors directed to the active site covalently label presenilin 1. *Nature* **405**, 689-694 (2000).

8 Steiner, H., Kostka, M., Romig, H., Basset, G., Pesold, B., Hardy, J., Capell, A., Meyn, L., Grim, M. G., Baumeister, R., Fechteler, K. & Haass, C. Glycine 384 is required for presenilin-1 function and is conserved in polytopic bacterial aspartyl proteases. *Nat. Cell Biol.* **2**, 848-851 (2000).

9 Steiner, H., Duff, K., Capell, A., Romig, H., Grim, M. G., Lincoln, S., Hardy, J., Yu, X., Picciano, M., Fechteler, K., Citron, M., Kopan, R., Pesold, B., Keck, S., Baader, M., Tomita, T., Iwatsubo, T., Baumeister, R. & Haass, C. A loss of function mutation of presenilin-2 interferes with amyloid β-peptide production and Notch signaling. *J. Biol. Chem.* **274**, 28669-28673 (1999).

10 Kimberly, W. T., Xia, W., Rahmati, T., Wolfe, M. S. & Selkoe, D. J. The transmembrane aspartates in presenilin 1 and 2 are obligatory for γ-secretase activity and amyloid β-protein generation. *J. Biol. Chem.* **275**, 3173-3178 (2000).

11 Yu, G., Chen, F., Levesque, G., Nishimura, M., Zhang, D. M., Levesque, L., Rogaeva, E., Xu, D., Liang, Y., Duthie, M., St George-Hyslop, P. H. & Fraser, P. E. The presenilin 1 protein is a component of a high molecular weight intracellular complex that contains β-catenin. *J. Biol. Chem.* **273**, 16470-16475 (1998).

12 Saura, C. A., Tomita, T., Davenport, F., Harris, C. L., Iwatsubo, T. & Thinakaran, G. Evidence that intramolecular associations between presenilin domains are obligatory for endoproteolytic processing. *J. Biol. Chem.* **274**, 13818-13823 (1999).

13 Weihofen, A., Binns, K., Lemberg, M. K., Ashman, K. & Martoglio, B. Identification of signal peptide peptidase, a presenilin-type aspartic protease. *Science* **296**, 2215-2218 (2002).

14 Ponting, C. P., Hutton, M., Nyborg, A., Baker, M., Jansen, K. & Golde, T. E. Identification of a novel family of presenilin homologues. *Hum. Mol. Genet.* **11**, 1037-1044 (2002).

15 Torres-Arancivia, C., Ross, C. M., Chavez, J., Assur, Z., Dolios, G., Mancia, F. & Ubarretxena-Belandia, I. Identification of an archaeal presenilin-like intramembrane protease. *PLoS One* **5** (2010).

16 Dang, S., Wu, S., Wang, J., Li, H., Huang, M., He, W., Li, Y. M., Wong, C. C. & Shi, Y. Cleavage of amyloid precursor protein by an archaeal presenilin homologue PSH. *Proc. Natl. Acad. Sci. USA* **112**, 3344-3349 (2015).

17 Naing, S. H., Vukoti, K. M., Drury, J. E., Johnson, J. L., Kalyoncu, S., Hill, S. E., Torres, M. P. & Lieberman, R. L. Catalytic properties of intramembrane aspartyl protease substrate hydrolysis evaluated using a FRET peptide cleavage assay. *ACS Chem. Biol.* **10**, 2166-2174 (2015).

18 Naing, S. H., Kalyoncu, S., Smalley, D. M., Kim, H., Tao, X., George, J. B., Jonke, A. P., Oliver, R. C., Urban, V. S., Torres, M. P. & Lieberman, R. L. Both positional and chemical variables control in vitro proteolytic cleavage of a presenilin ortholog. *J. Biol. Chem.* **293**, 4653-4663 (2018).

19 Takami, M., Nagashima, Y., Sano, Y., Ishihara, S., Morishima-Kawashima, M., Funamoto, S. & Ihara, Y. γ-Secretase: successive tripeptide and tetrapeptide release from the transmembrane domain of β-carboxyl terminal fragment. *J. Neurosci.* **29**, 13042-13052 (2009).

20 Takasugi, N., Tomita, T., Hayashi, I., Tsuruoka, M., Niimura, M., Takahashi, Y., Thinakaran, G. & Iwatsubo, T. The role of presenilin cofactors in the γ-secretase complex. *Nature* **422**, 438-441 (2003).

21 Edbauer, D., Winkler, E., Regula, J. T., Pesold, B., Steiner, H. & Haass, C. Reconstitution of γ-secretase activity. *Nat. Cell Biol.* **5**, 486-488 (2003).

22 Kimberly, W. T., LaVoie, M. J., Ostaszewski, B. L., Ye, W., Wolfe, M. S. & Selkoe, D. J. γ-Secretase is a membrane protein complex comprised of presenilin, nicastrin, Aph-1, and Pen-2. *Proc. Natl. Acad. Sci. USA* **100**, 6382-6387 (2003).

23 Li, X., Dang, S., Yan, C., Gong, X., Wang, J. & Shi, Y. Structure of a presenilin family intramembrane aspartate protease. *Nature* **493**, 56-61 (2013).

24 Sun, L., Zhao, L., Yang, G., Yan, C., Zhou, R., Zhou, X., Xie, T., Zhao, Y., Wu, S., Li, X. & Shi, Y. Structural basis of human γ-secretase assembly. *Proc. Natl. Acad. Sci. USA* **112**, 6003-6008 (2015).

25 Bai, X. C., Yan, C., Yang, G., Lu, P., Ma, D., Sun, L., Zhou, R., Scheres, S. H. & Shi, Y. An atomic structure of human γ-secretase. *Nature* **525**, 212-217 (2015).

26 Zhou, R., Yang, G., Guo, X., Zhou, Q., Lei, J. & Shi, Y. Recognition of the amyloid precursor protein by human γ-secretase. *Science* **363**, aaw0930 (2019).

27 Yang, G., Zhou, R., Zhou, Q., Guo, X., Yan, C., Ke, M., Lei, J. & Shi, Y. Structural basis of Notch recognition by human γ-secretase. *Nature* **565**, 192-197 (2019).

28 Bai, X. C., Rajendra, E., Yang, G., Shi, Y. & Scheres, S. H. Sampling the conformational space of the catalytic subunit of human γ-secretase. *eLife* **4**, e11182 (2015).

29 Yang, G., Zhou, R., Guo, X., Yan, C., Lei, J. & Shi, Y. Structural basis of γ-secretase inhibition and modulation by small molecule drugs. *Cell* **184**, 521-533 e514 (2021).

30 Paschkowsky, S., Oestereich, F. & Munter, L. M. Embedded in the membrane: How lipids confer activity and specificity to intramembrane proteases. *J. Membr. Biol.* **251**, 369-378 (2018).

31 Zhou, H., Zhou, S., Walian, P. J. & Jap, B. K. Dependency of γ-secretase complex activity on the structural integrity of the bilayer. *Biochem. Biophys. Res. Commun.* **402**, 291-296 (2010).

32 Shearman, M. S., Beher, D., Clarke, E. E., Lewis, H. D., Harrison, T., Hunt, P., Nadin, A., Smith, A. L., Stevenson, G. & Castro, J. L. L-685,458, an aspartyl protease transition state mimic, is a potent inhibitor of amyloid β-protein precursor γ-secretase activity. *Biochemistry* **39**, 8698-8704. (2000).

33 Osenkowski, P., Ye, W., Wang, R., Wolfe, M. S. & Selkoe, D. J. Direct and potent regulation of γ-secretase by its lipid microenvironment. *J. Biol. Chem.* **283**, 22529-22540 (2008).

34 Osawa, S., Funamoto, S., Nobuhara, M., Wada-Kakuda, S., Shimojo, M., Yagishita, S. & Ihara, Y. Phosphoinositides suppress γ-secretase in both the detergent-soluble and -insoluble states. *J. Biol. Chem.* **283**, 19283-19292 (2008).

35 Holmes, O., Paturi, S., Ye, W., Wolfe, M. S. & Selkoe, D. J. Effects of membrane lipids on the activity and processivity of purified γ-secretase. *Biochemistry* **51**, 3565-3575 (2012).

36 Winkler, E., Kamp, F., Scheuring, J., Ebke, A., Fukumori, A. & Steiner, H. Generation of Alzheimer disease-associated amyloid β42/43 peptide by γ-secretase can be inhibited directly by modulation of membrane thickness. *J. Biol. Chem.* **287**, 21326-21334 (2012).

37 Quintero-Monzon, O., Martin, M. M., Fernandez, M. A., Cappello, C. A., Krzysiak, A. J., Osenkowski, P. & Wolfe, M. S. Dissociation between the processivity and total activity of γ-secretase: implications for the mechanism of Alzheimer's disease-causing presenilin mutations. *Biochemistry* **50**, 9023-9035 (2011).

38 Lichtenthaler, S. F., Haass, C. & Steiner, H. Regulated intramembrane proteolysis--lessons from amyloid precursor protein processing. *J Neurochem* **117**, 779-796 (2011).

39 Kucerka, N., Nieh, M. P. & Katsaras, J. Fluid phase lipid areas and bilayer thicknesses of commonly used phosphatidylcholines as a function of temperature. *Biochim Biophys Acta* **1808**, 2761-2771 (2011).

40 Sun, L., Zhou, R., Yang, G. & Shi, Y. Analysis of 138 pathogenic mutations in presenilin-1 on the in vitro production of Aβ42 and Aβ40 peptides by γ-secretase. *Proc Natl Acad Sci U S A* **114**, E476-E485 (2017).

41 Chen, S. Y. & Zacharias, M. How mutations perturb γ-secretase active site studied by free energy simulations. *ACS Chem. Neurosci.* (2020).

42 Beher, D., Fricker, M., Nadin, A., Clarke, E. E., Wrigley, J. D., Li, Y. M., Culvenor, J. G., Masters, C. L., Harrison, T. & Shearman, M. S. In vitro characterization of the presenilin-dependent gamma-secretase complex using a novel affinity ligand. *Biochemistry* **42**, 8133-8142 (2003).

43 Esler, W. P., Kimberly, W. T., Ostaszewski, B. L., Ye, W., Diehl, T. S., Selkoe, D. J. & Wolfe, M. S. Activity-dependent isolation of the presenilin–γ-secretase complex reveals nicastrin and a γ substrate. *Proc. Natl. Acad. Sci. USA* **99**, 2720-2725 (2002).

44 Dovey, H. F., John, V., Anderson, J. P., Chen, L. Z., de Saint Andrieu, P., Fang, L. Y., Freedman, S. B., Folmer, B., Goldbach, E., Holsztynska, E. J., Hu, K. L., Johnson-Wood, K. L., Kennedy, S. L., Kholodenko, D., Knops, J. E., Latimer, L. H., Lee, M., Liao, Z., Lieberburg, I. M., Motter, R. N., Mutter, L. C., Nietz, J., Quinn, K. P., Sacchi, K. L., Seubert, P. A., Shopp, G. M., Thorsett, E. D., Tung, J. S., Wu, J., Yang, S., Yin, C. T., Schenk, D. B., May, P. C., Altstiel, L. D., Bender, M. H., Boggs, L. N., Britton, T. C., Clemens, J. C., Czilli, D. L., Dieckman-McGinty, D. K., Droste, J. J., Fuson, K. S., Gitter, B. D., Hyslop, P. A., Johnstone, E. M., Li, W. Y., Little, S. P., Mabry, T. E., Miller, F. D. & Audia, J. E. Functional γ-secretase inhibitors reduce β-amyloid peptide levels in brain. *J. Neurochem.* **76**, 173-181. (2001).

45 Lanz, T. A., Hosley, J. D., Adams, W. J. & Merchant, K. M. Studies of Aβ pharmacodynamics in the brain, cerebrospinal fluid, and plasma in young (plaque-free) Tg2576 mice using the γ-secretase inhibitor N2-[(2S)-2-(3,5-difluorophenyl)-2-hydroxyethanoyl]-N1-[(7S)-5-methyl-6-oxo-6,7-di hydro-5H-

dibenzo[b,d]azepin-7-yl]-L-alaninamide (LY-411575). *J Pharmacol Exp Ther* **309**, 49-55 (2004).

46 Mayer, S. C., Kreft, A. F., Harrison, B., Abou-Gharbia, M., Antane, M., Aschmies, S., Atchison, K., Chlenov, M., Cole, D. C., Comery, T., Diamantidis, G., Ellingboe, J., Fan, K., Galante, R., Gonzales, C., Ho, D. M., Hoke, M. E., Hu, Y., Huryn, D., Jain, U., Jin, M., Kremer, K., Kubrak, D., Lin, M., Lu, P., Magolda, R., Martone, R., Moore, W., Oganesian, A., Pangalos, M. N., Porte, A., Reinhart, P., Resnick, L., Riddell, D. R., Sonnenberg-Reines, J., Stock, J. R., Sun, S. C., Wagner, E., Wang, T., Woller, K., Xu, Z., Zaleska, M. M., Zeldis, J., Zhang, M., Zhou, H. & Jacobsen, J. S. Discovery of begacestat, a Notch-1-sparing γ-secretase inhibitor for the treatment of Alzheimer's disease. *J. Med. Chem.* **51**, 7348-7351 (2008).

47 Best, J. D., Jay, M. T., Otu, F., Churcher, I., Reilly, M., Morentin-Gutierrez, P., Pattison, C., Harrison, T., Shearman, M. S. & Atack, J. R. In vivo characterization of Aβ(40) changes in brain and cerebrospinal fluid using the novel γ-secretase inhibitor N-[cis-4-[(4-chlorophenyl)sulfonyl]-4-(2,5-difluorophenyl)cyclohexyl]-1,1,1-trifl uoromethanesulfonamide (MRK-560) in the rat. *J Pharmacol Exp Ther* **317**, 786-790 (2006).

48 Hitzenberger, M. & Zacharias, M. Uncovering the binding mode of γ-secretase Inhibitors. *ACS Chem. Neurosci.* **10**, 3398-3403 (2019).

49 Mehra, R., Dehury, B. & Kepp, K. P. Cryo-temperature effects on membrane protein structure and dynamics. *Phys. Chem. Chem. Phys.* **22**, 5427-5438 (2020).

50 Bhattarai, A., Devkota, S., Bhattarai, S., Wolfe, M. S. & Miao, Y. Mechanisms of γ-secretase activation and substrate processing. *ACS Cent. Sci.* **6**, 969-983 (2020).

51 Okochi, M., Tagami, S., Yanagida, K., Takami, M., Kodama, T. S., Mori, K., Nakayama, T., Ihara, Y. & Takeda, M. γ-Secretase modulators and presenilin 1 mutants act differently on presenilin/γ-secretase function to cleave Aβ42 and Aβ43. *Cell Rep.* **3**, 42-51 (2013).

52 Dehury, B., Tang, N. & Kepp, K. P. Molecular dynamics of C99-bound γ-secretase reveal two binding modes with distinct compactness, stability, and active-site retention: implications for Aβ production. *Biochem. J.* **476**, 1173-1189 (2019).

53 Szaruga, M., Munteanu, B., Lismont, S., Veugelen, S., Horre, K., Mercken, M., Saido, T. C., Ryan, N. S., De Vos, T., Savvides, S. N., Gallardo, R., Schymkowitz, J., Rousseau, F., Fox, N. C., Hopf, C., De Strooper, B. & Chavez-Gutierrez, L. Alzheimer's-causing mutations shift Aβ length by destabilizing γ-secretase-Aβn Interactions. *Cell* **170**, 443-456 e414 (2017).

54 Somavarapu, A. K. & Kepp, K. P. Loss of stability and hydrophobicity of presenilin 1 mutations causing Alzheimer's disease. *J. Neurochem.* **137**, 101-111 (2016).

55 Tang, N., Dehury, B. & Kepp, K. P. Computing the Pathogenicity of Alzheimer's Disease Presenilin 1 Mutations. *J. Chem. Inf. Model* **59**, 858-870 (2019).

56 Fukumori, A. & Steiner, H. Substrate recruitment of γ-secretase and mechanism of clinical presenilin mutations revealed by photoaffinity mapping. *EMBO J.* **35**, 1628-1643 (2016).

57 Trambauer, J., Rodriguez Sarmiento, R. M., Fukumori, A., Feederle, R., Baumann, K. & Steiner, H. Aβ43-producing PS1 FAD mutants cause altered substrate interactions and respond to γ-secretase modulation. *EMBO Rep.* **21**, e47996 (2020).

58 Hu, J., Xue, Y., Lee, S. & Ha, Y. The crystal structure of GXGD membrane protease FlaK. *Nature* **475**, 528-531 (2011).

59 Case, D. A., Cheatham, T. E., 3rd, Darden, T., Gohlke, H., Luo, R., Merz, K. M., Jr., Onufriev, A., Simmerling, C., Wang, B. & Woods, R. J. The Amber biomolecular simulation programs. *J. Comput. Chem.* **26**, 1668-1688 (2005).

60 Jo, S., Kim, T., Iyer, V. G. & Im, W. CHARMM-GUI: a web-based graphical user interface for CHARMM. *J. Comput. Chem.* **29**, 1859-1865 (2008).

61 Waterhouse, A., Bertoni, M., Bienert, S., Studer, G., Tauriello, G., Gumienny, R., Heer, F. T., de Beer, T. A. P., Rempfer, C., Bordoli, L., Lepore, R. & Schwede, T. SWISS-MODEL: homology modelling of protein structures and complexes. *Nucleic Acids Res.* **46**, W296-W303 (2018).

62 Olsson, M. H., Sondergaard, C. R., Rostkowski, M. & Jensen, J. H. PROPKA3: Consistent treatment of internal and surface residues in empirical pKa predictions. *J. Chem. Theory Comput.* **7**, 525-537 (2011).

1367 63 Sondergaard, C. R., Olsson, M. H., Rostkowski, M. & Jensen, J. H. Improved
1368 treatment of ligands and coupling effects in empirical calculation and
1369 rationalization of pKa values. *J. Chem. Theory Comput.* **7**, 2284-2295 (2011).

1370 64 Kabsch, W. & Sander, C. Dictionary of protein secondary structure: pattern
1371 recognition of hydrogen-bonded and geometrical features. *Biopolymers* **22**,
1372 2577-2637 (1983).

1373 65 Touw, W. G., Baakman, C., Black, J., te Beek, T. A., Krieger, E., Joosten, R. P.
1374 & Vriend, G. A series of PDB-related databanks for everyday needs. *Nucleic*
1375 *Acids Res.* **43**, D364-368 (2015).

1376 66 Schagger, H. & von Jagow, G. Blue native electrophoresis for isolation of
1377 membrane protein complexes in enzymatically active form. *Anal. Biochem.*
1378 **199**, 223-231 (1991).

1379 67 Winkler, E., Hobson, S., Fukumori, A., Dumpelfeld, B., Luebbers, T., Baumann,
1380 K., Haass, C., Hopf, C. & Steiner, H. Purification, pharmacological modulation,
1381 and biochemical characterization of interactors of endogenous human γ-
1382 secretase. *Biochemistry* **48**, 1183-1197 (2009).

1383 68 Page, R. M., Baumann, K., Tomioka, M., Perez-Revuelta, B. I., Fukumori, A.,
1384 Jacobsen, H., Flohr, A., Luebbers, T., Ozmen, L., Steiner, H. & Haass, C.
1385 Generation of Aβ38 and Aβ42 is independently and differentially affected by
1386 FAD-associated presenilin 1 mutations and γ-secretase modulation. *J. Biol.*
1387 *Chem.* **283**, 677-683 (2008).

69 Ebke, A., Luebbers, T., Fukumori, A., Shirotani, K., Haass, C., Baumann, K. & Steiner, H. Novel γ-secretase enzyme modulators directly target presenilin protein. *J. Biol. Chem.* **286**, 37181-37186 (2011).

70 Eswar, N., Webb, B., Marti-Renom, M. A., Madhusudhan, M. S., Eramian, D., Shen, M. Y., Pieper, U. & Sali, A. Comparative protein structure modeling using Modeller. *Curr. Protoc. Bioinformatics* **Chapter 5**, Unit-5 6 (2006).

71 Jorgensen, W. L., Chandrasekhar, J., Madura, J. D., Impey, R. W. & Klein, M. L. Comparison of simple potential functions for simulating liquid water. *J. Chem. Phys.* **79**, 926-935 (1983).

72 Cheng, X., Jo, S., Lee, H. S., Klauda, J. B. & Im, W. CHARMM-GUI micelle builder for pure/mixed micelle and protein/micelle complex systems. *J. Chem. Inf. Model* **53**, 2171-2180 (2013).

73 Wu, E. L., Cheng, X., Jo, S., Rui, H., Song, K. C., Davila-Contreras, E. M., Qi, Y., Lee, J., Monje-Galvan, V., Venable, R. M., Klauda, J. B. & Im, W. CHARMM-GUI Membrane Builder toward realistic biological membrane simulations. *J. Comput. Chem.* **35**, 1997-2004 (2014).

74 Huang, J., Rauscher, S., Nawrocki, G., Ran, T., Feig, M., de Groot, B. L., Grubmuller, H. & MacKerell, A. D., Jr. CHARMM36m: an improved force field for folded and intrinsically disordered proteins. *Nat. Methods* **14**, 71-73 (2017).

75 Tieleman, D. P., Marrink, S. J. & Berendsen, H. J. A computer perspective of membranes: molecular dynamics studies of lipid bilayer systems. *Biochim. Biophys. Acta* **1331**, 235-270 (1997).

76 Vermeer, L. S., de Groot, B. L., Reat, V., Milon, A. & Czaplicki, J. Acyl chain order parameter profiles in phospholipid bilayers: computation from molecular dynamics simulations and comparison with 2H NMR experiments. *Eur. Biophys. J.* **36**, 919-931 (2007).

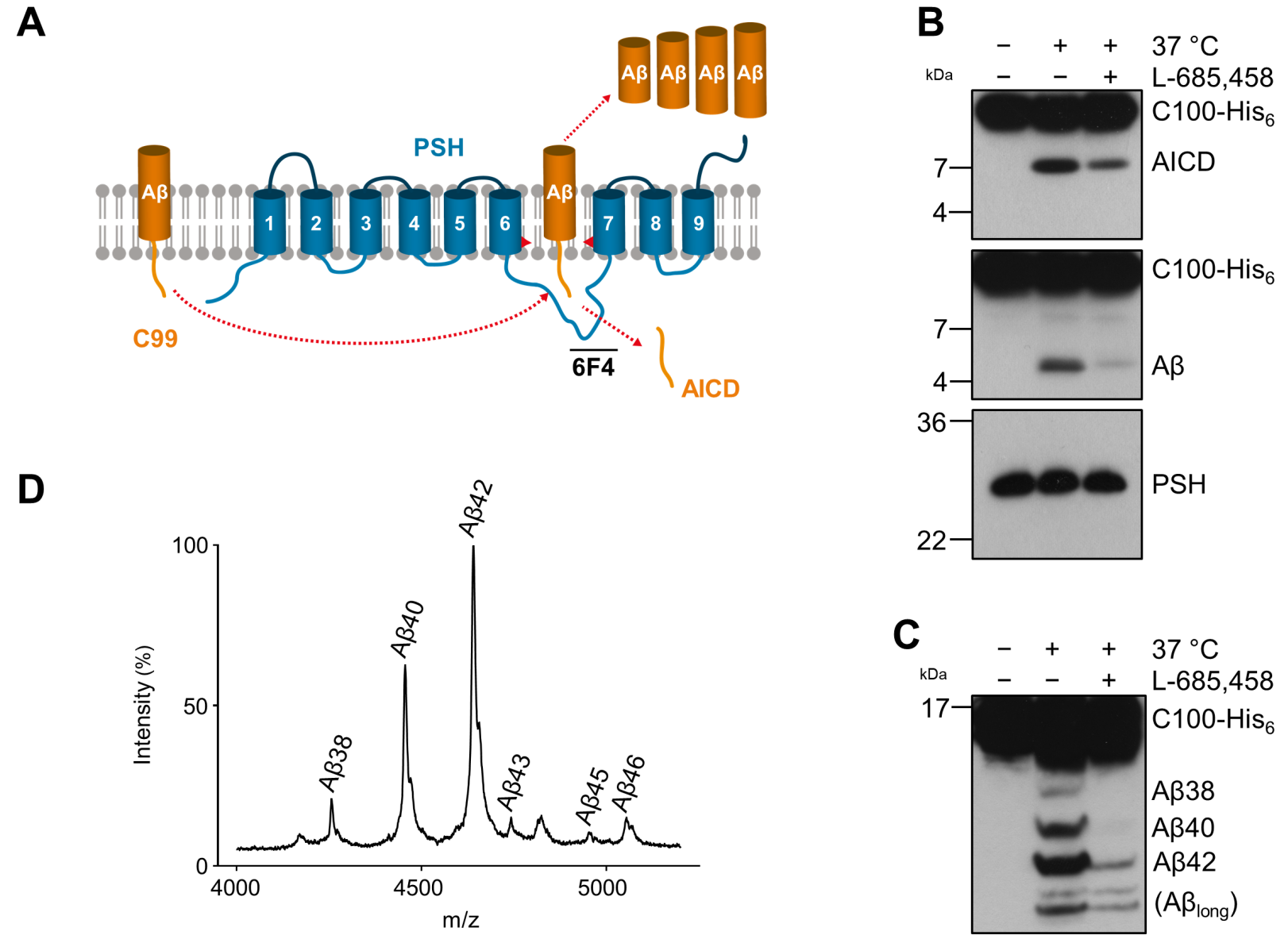
A
Aβ
Aβ
Aβ
Aβ
PSH
Aβ
1
2
3
4
5
6
7
8
9
C99
6F4
AICD
B
kDa
37 °C
L-685,458
C100-His6
AICD
7
4
C100-His6
Aβ
7
4
36
PSH
22
C
kDa
37 °C
L-685,458
17
C100-His6
Aβ38
Aβ40
Aβ42
(Aβlong)
D
Intensity (%)
100
50
0
Aβ38
Aβ40
Aβ42
Aβ43
Aβ45
Aβ46
4000
4500
5000
m/z

Figure 1

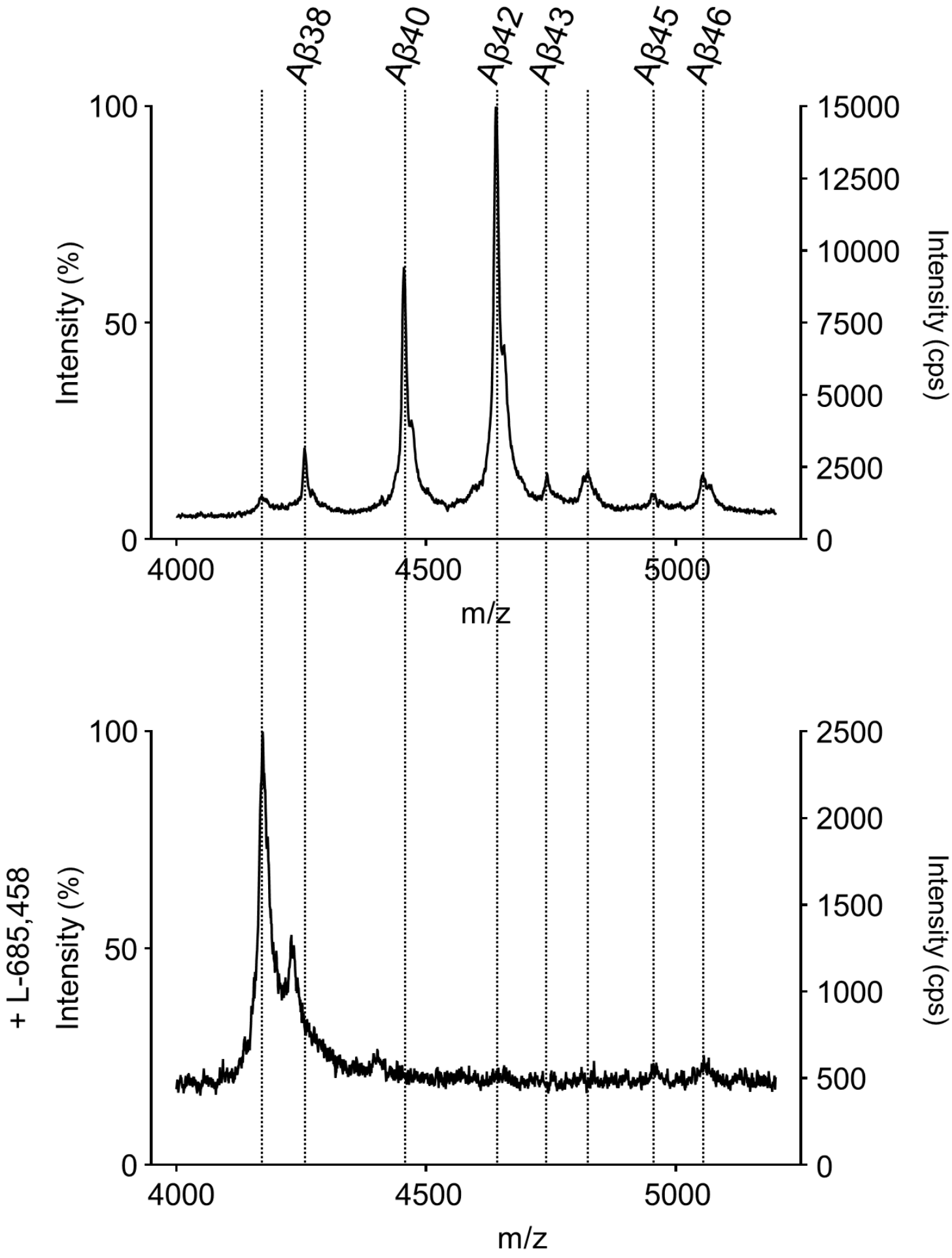

Figure 1 – figure supplement 1

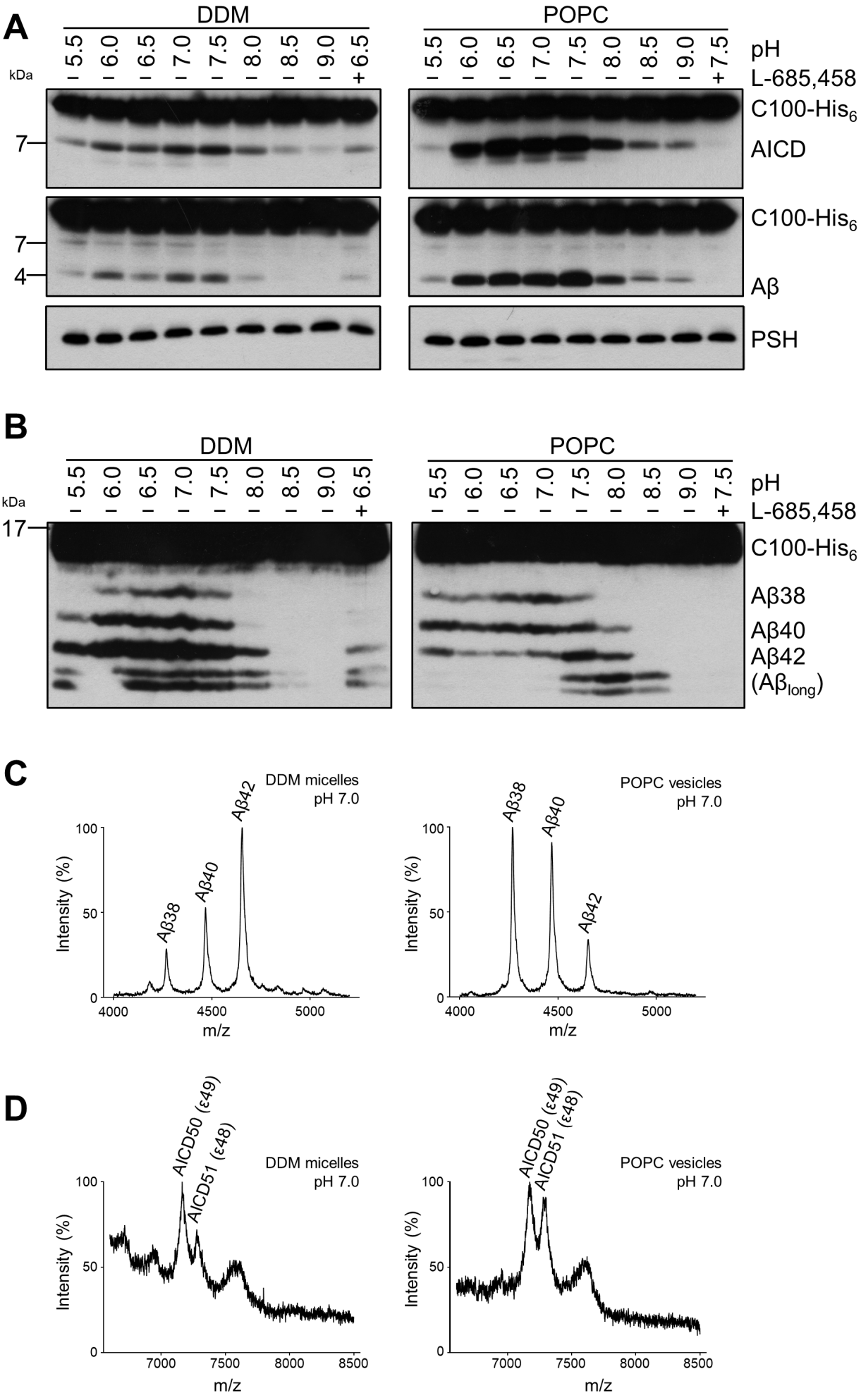
A
DDM
POPC
pH
5.5
6.0
6.5
7.0
7.5
8.0
8.5
9.0
6.5
7.5
kDa
L-685,458
C100-His6
AICD
Aβ
PSH
7
4
B
17
Aβ38
Aβ40
Aβ42
(Aβlong)
C
DDM micelles
pH 7.0
POPC vesicles
Intensity (%)
m/z
D
AICD50 (ε49)
AICD51 (ε48)

Figure 2

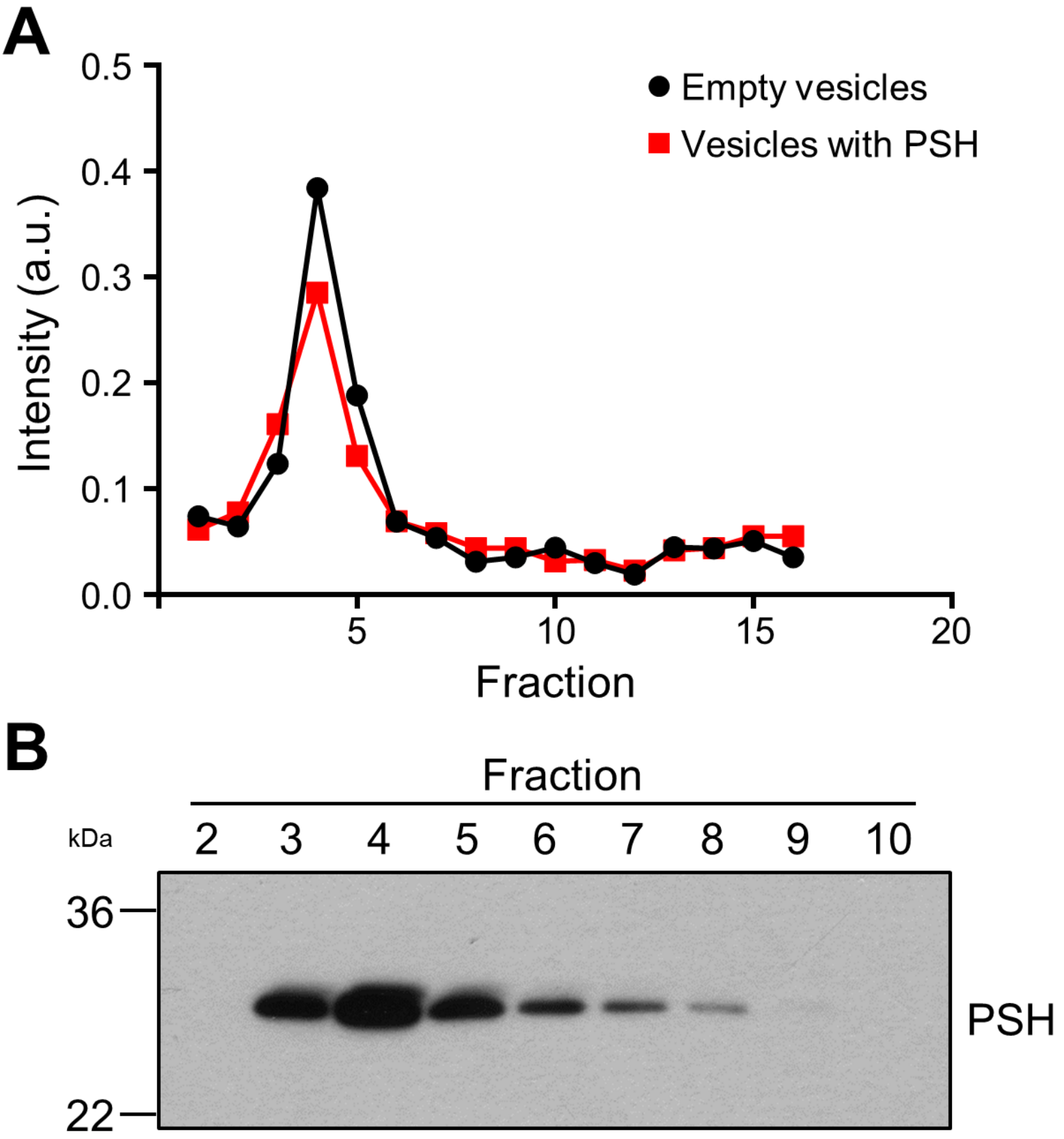

Figure 2 – figure supplement 1

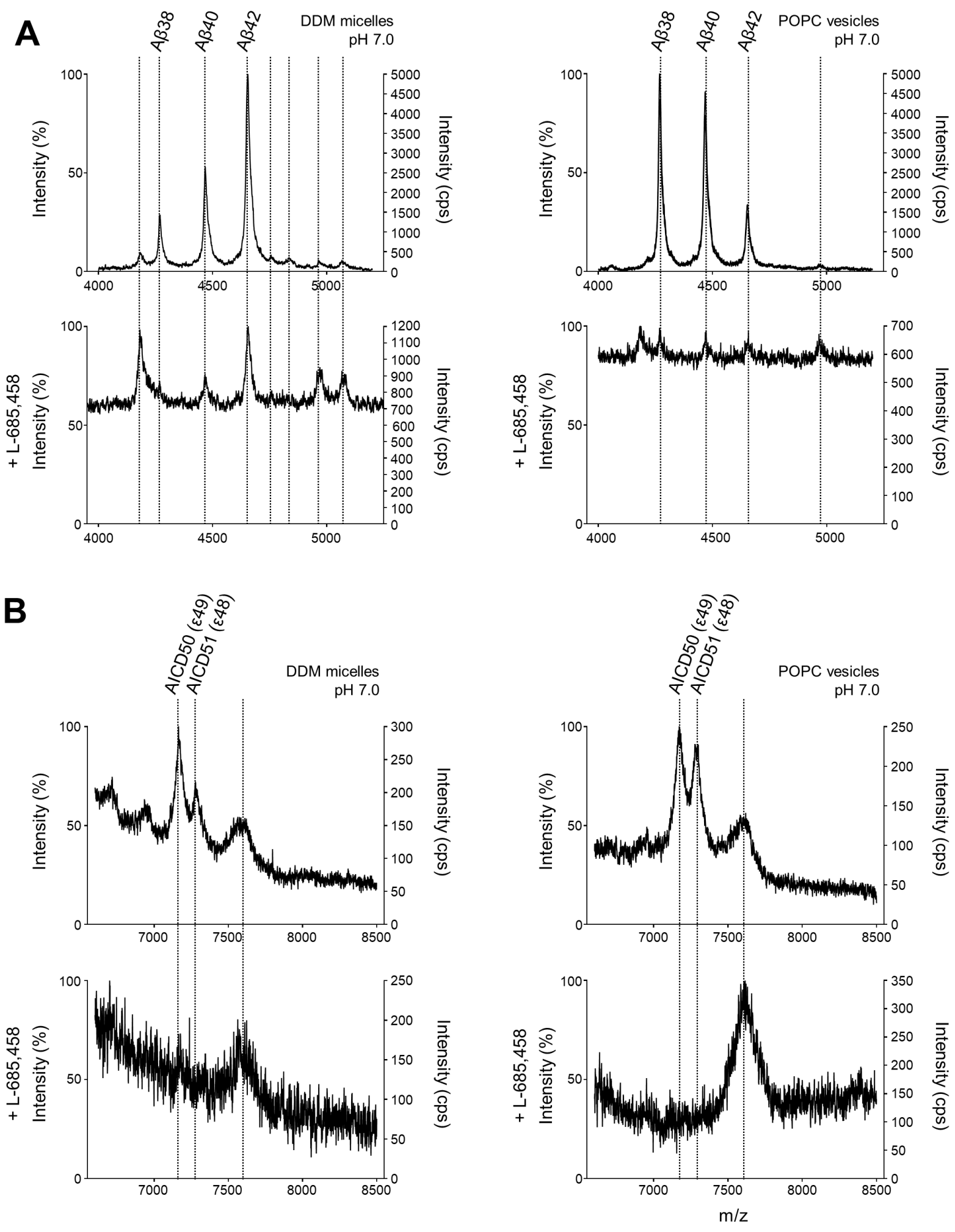

Figure 2 – figure supplement 2

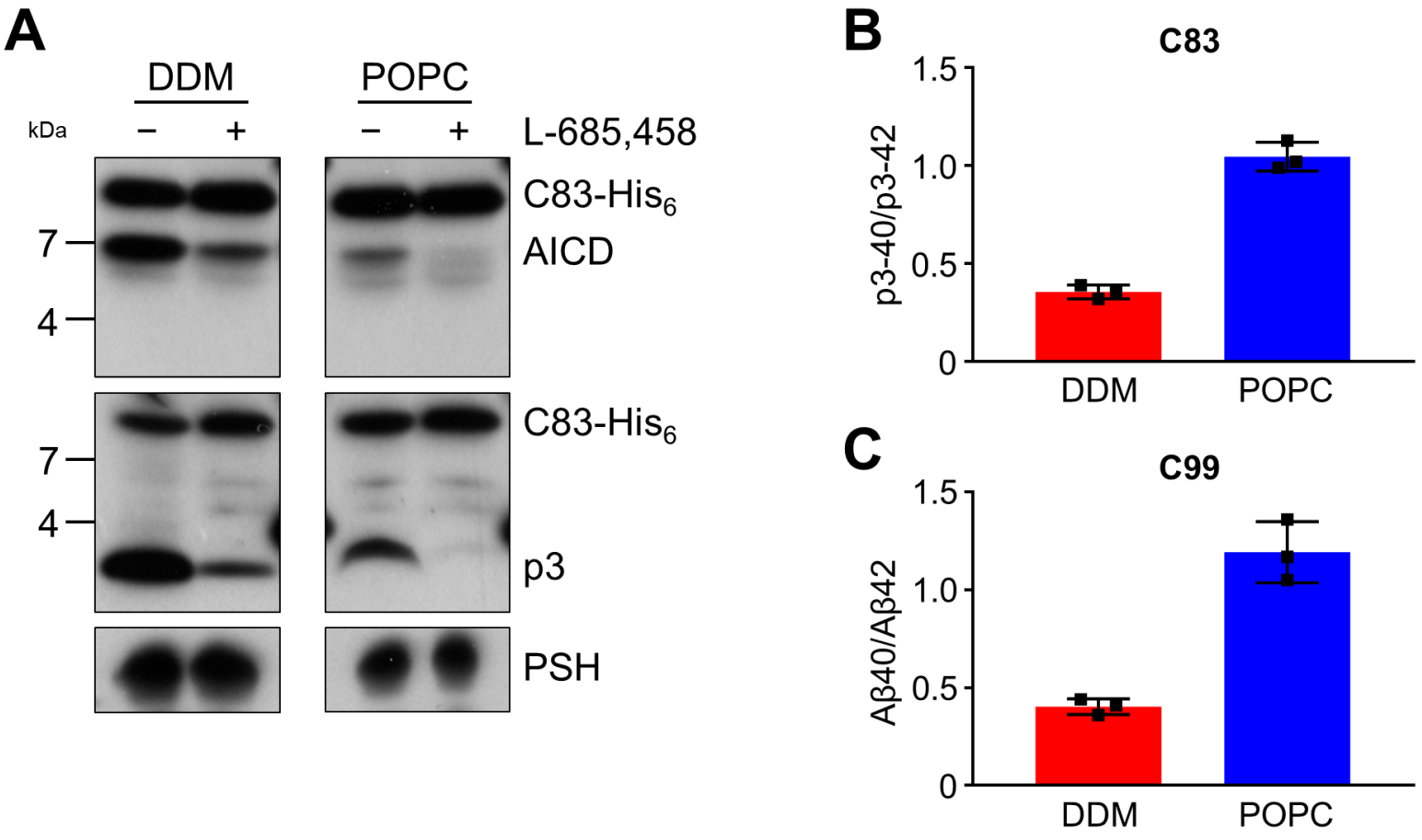
A
DDM
POPC
kDa
–
+
–
+
L-685,458
C83-His6
AICD
7
4
C83-His6
p3
PSH
B
C83
p3-40/p3-42
1.5
1.0
0.5
0
DDM
POPC
C
C99
Aβ40/Aβ42
1.5
1.0
0.5
0
DDM
POPC

Figure 3

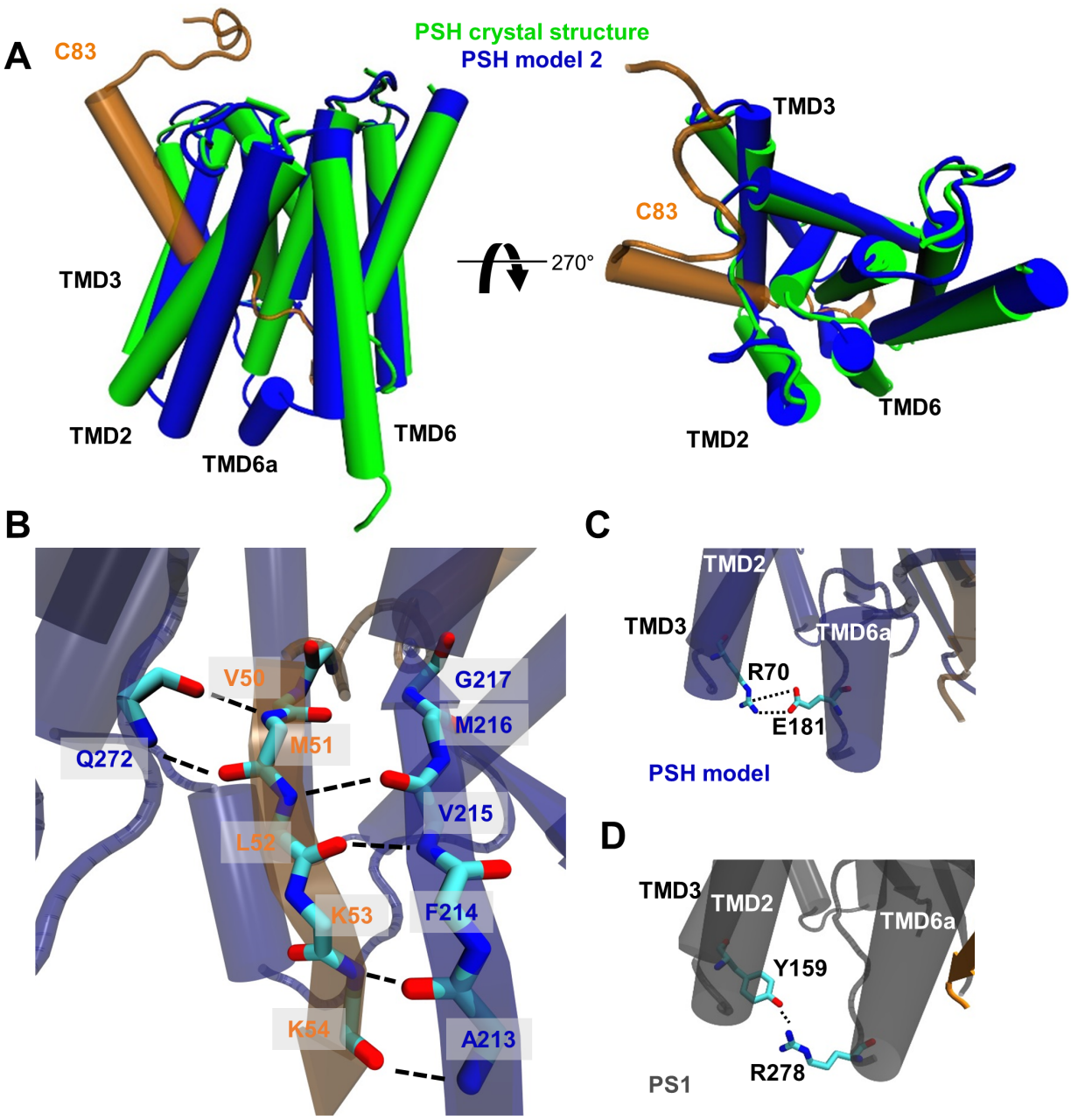
A
C83
PSH crystal structure
PSH model 2
TMD3
TMD2
TMD6a
TMD6
270°
C83
TMD3
TMD6
TMD2
B
V50
G217
M216
M51
Q272
V215
L52
K53
F214
K54
A213
C
TMD2
TMD3
TMD6a
R70
E181
PSH model
D
TMD3
TMD2
TMD6a
Y159
R278
PS1

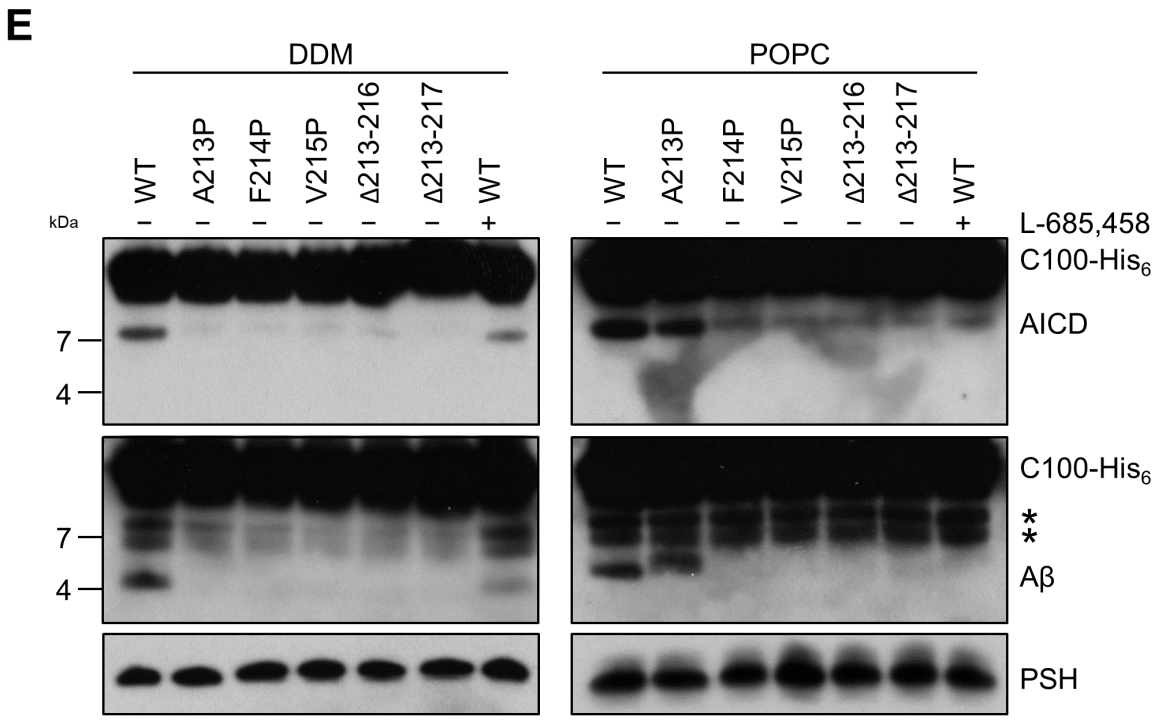
E
DDM
POPC
- WT
- A213P
- F214P
- V215P
- Δ213-216
- Δ213-217
+ WT
kDa
L-685,458
C100-His6
AICD
7
4
C100-His6
**
Aβ
PSH

Figure 4

A

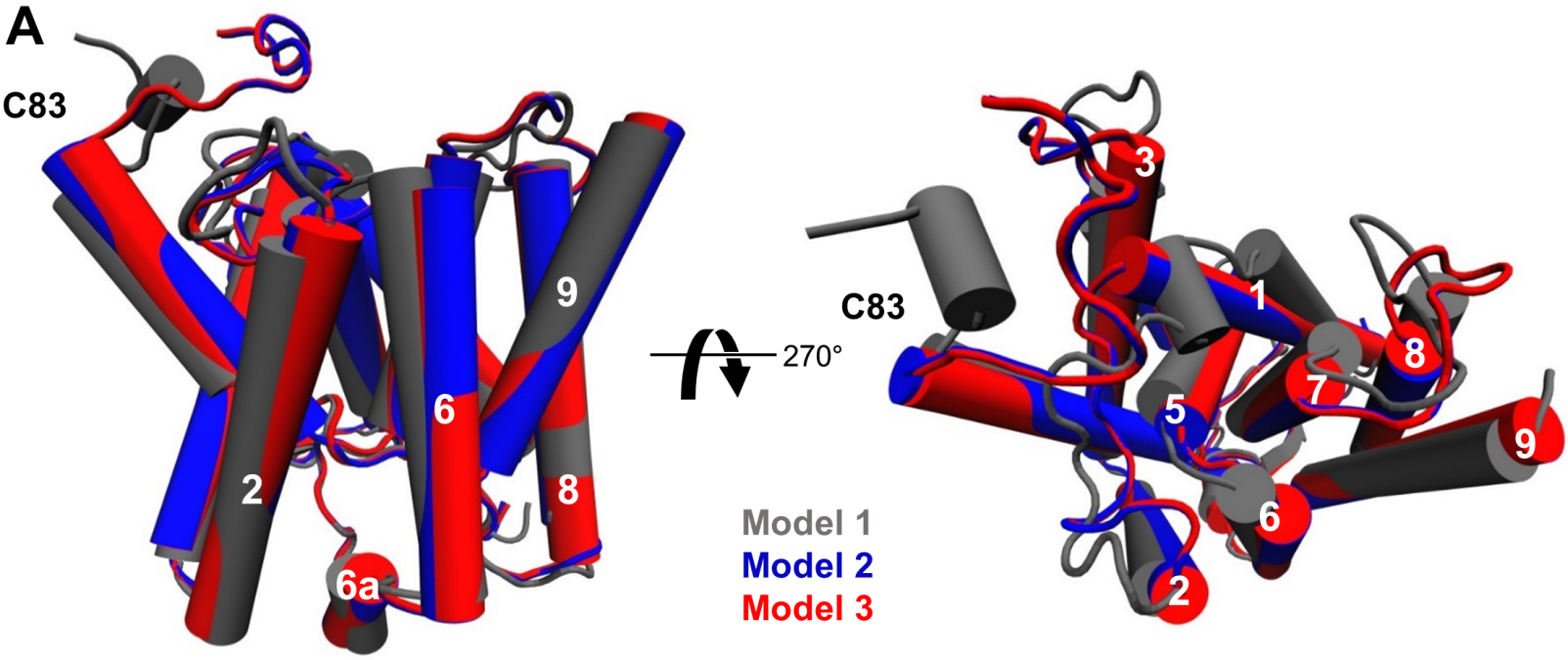

B

RMSD (Å)	4HYG (Chain B)	4Y6K (Chain B)	Model 1	Model 2	Model 3
4HYG (Chain B)	0				
4Y6K (Chain B)	0.349	0			
Model 1	3.379	3.349	0		
Model 2	1.153	1.602	1.355	0	
Model 3	1.416	1.513	1.484	0.163	0

Figure 4 – figure supplement 1

Figure 4 – figure supplement 2

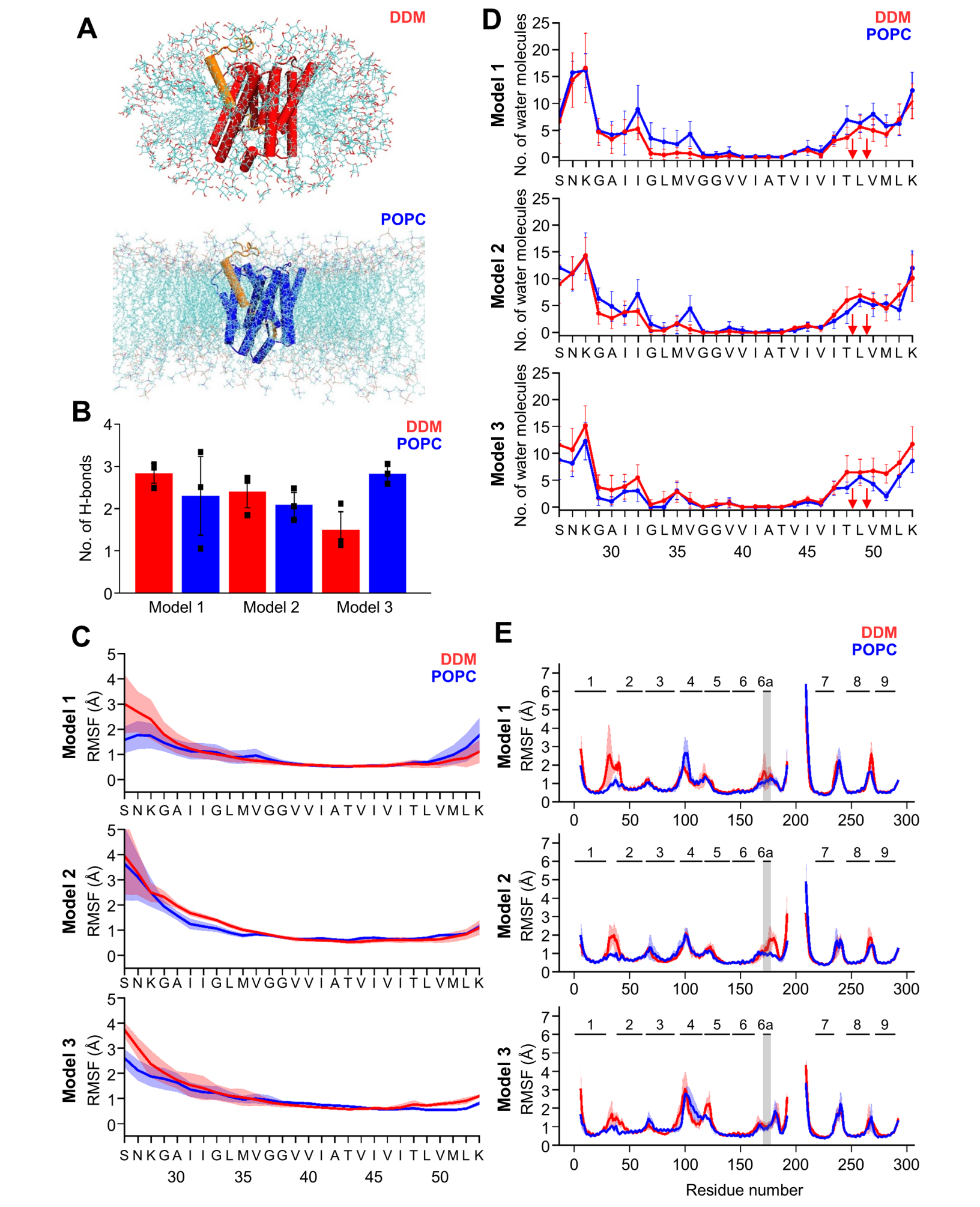
A
DDM
POPC
B
DDM
POPC
No. of H-bonds
Model 1
Model 2
Model 3
C
DDM
POPC
Model 1
Model 2
Model 3
RMSF (Å)
S N K G A I I G L M V G G V V I A T V I V I T L V M L K
30
35
40
45
50
D
DDM
POPC
Model 1
Model 2
Model 3
No. of water molecules
E
DDM
POPC
1
2
3
4
5
6
6a
7
8
9
Residue number

Figure 5

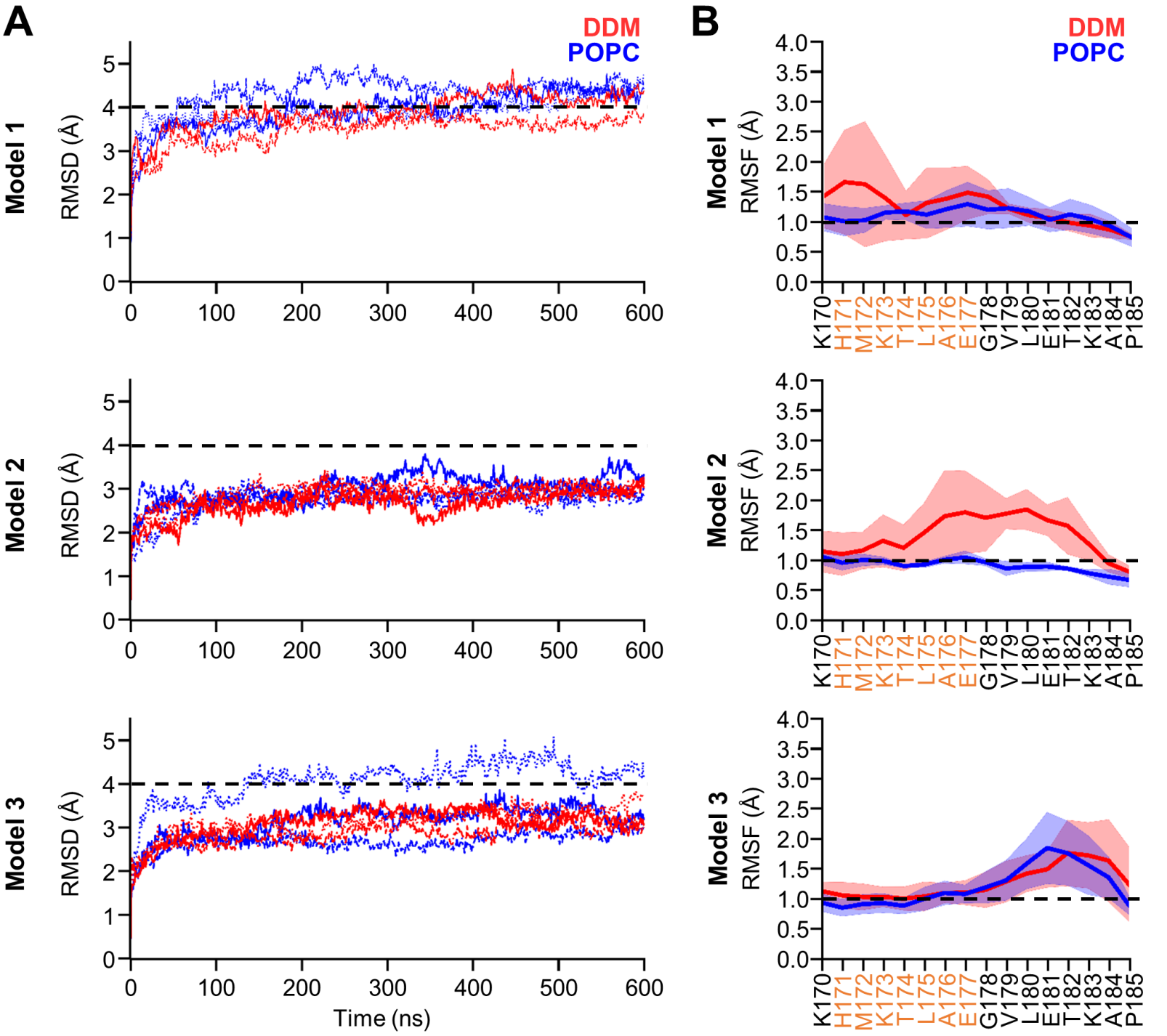

Figure 5 – figure supplement 1

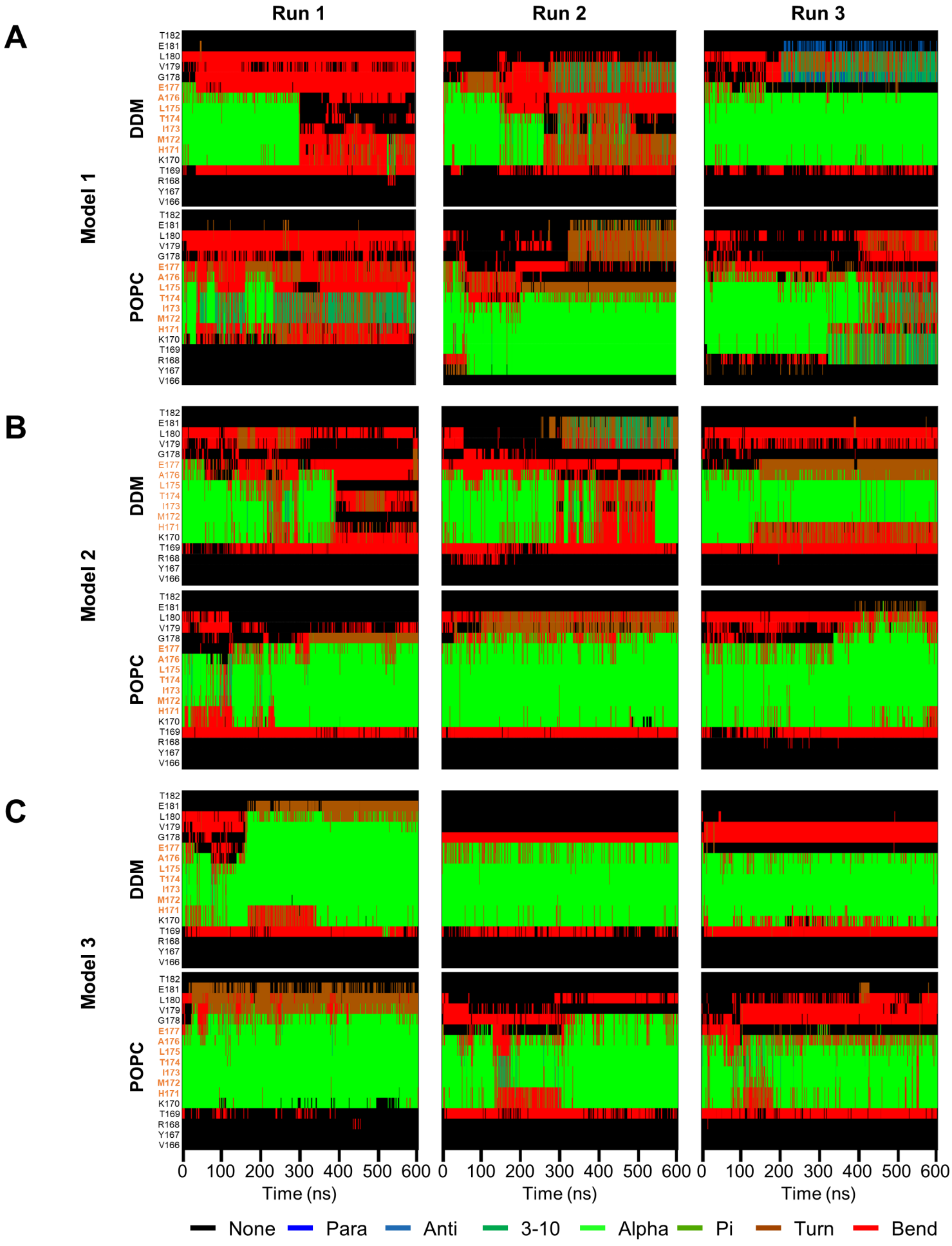

Figure 5 – figure supplement 2

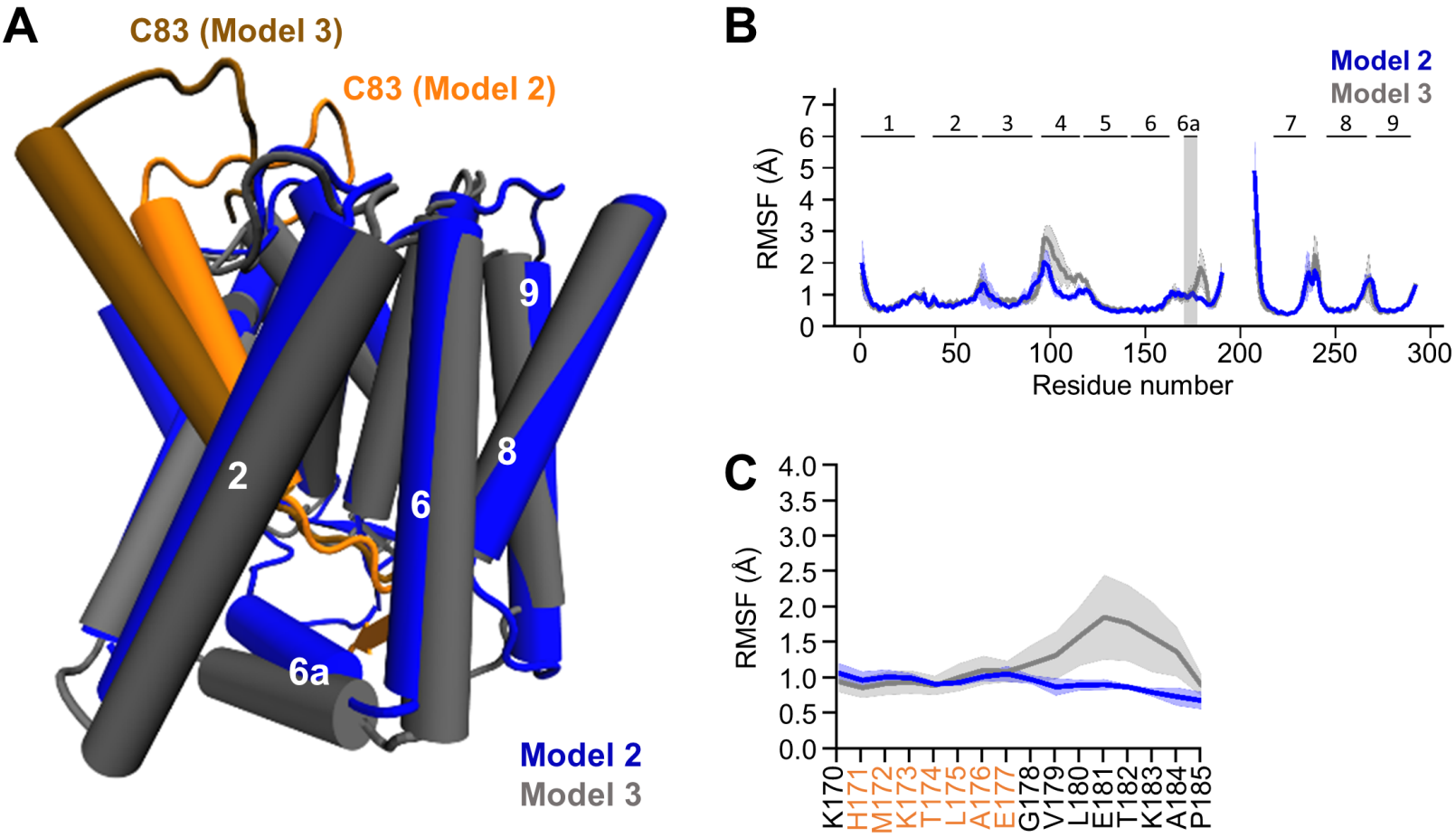

Figure 5 – figure supplement 3

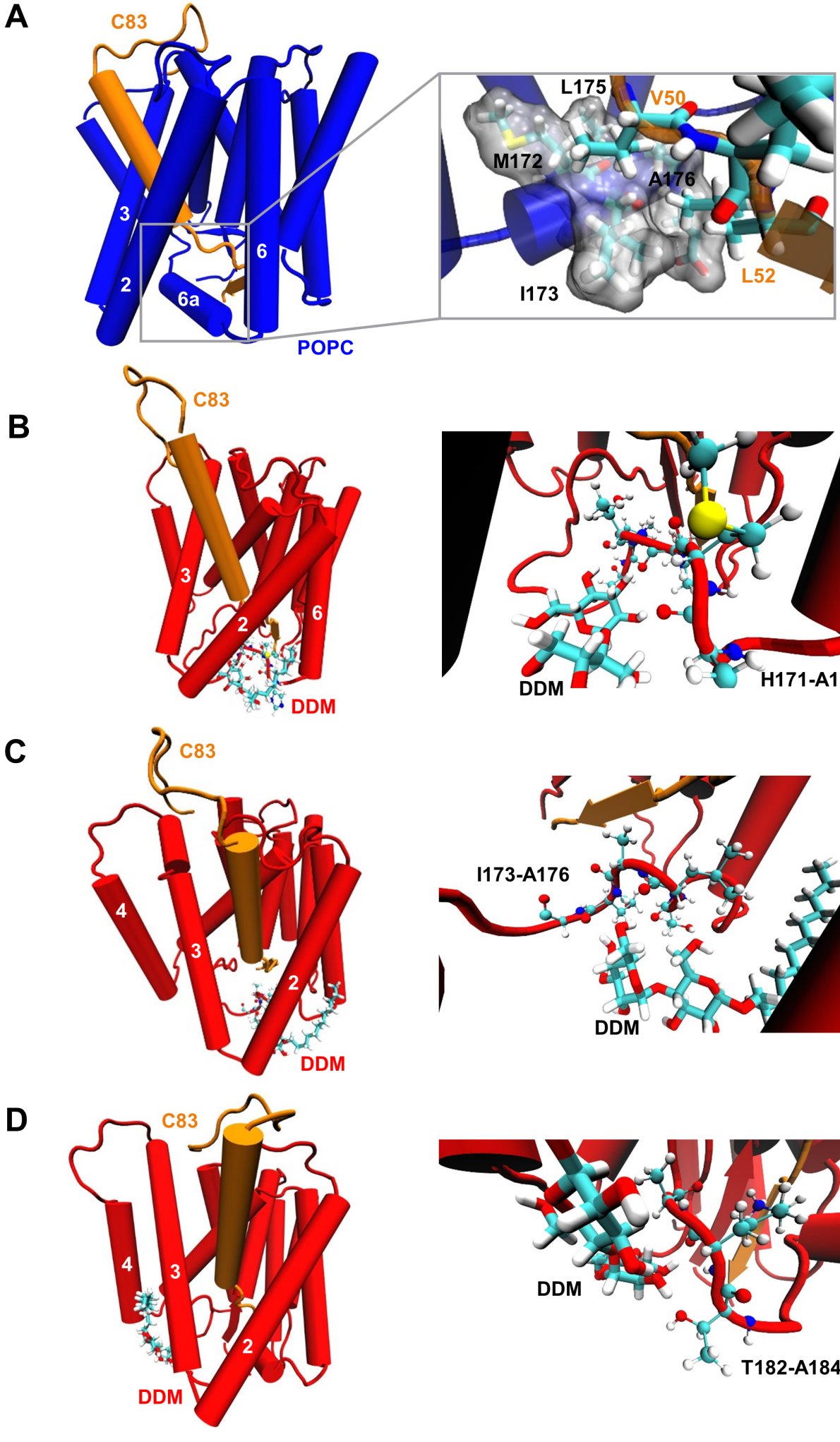
A
C83
3
6
2
6a
POPC
L175
V50
M172
A176
L52
I173
B
C83
3
2
6
DDM
DDM
H171-A176
C
C83
4
3
2
DDM
I173-A176
DDM
D
C83
4
3
2
DDM
DDM
T182-A184

Figure 6

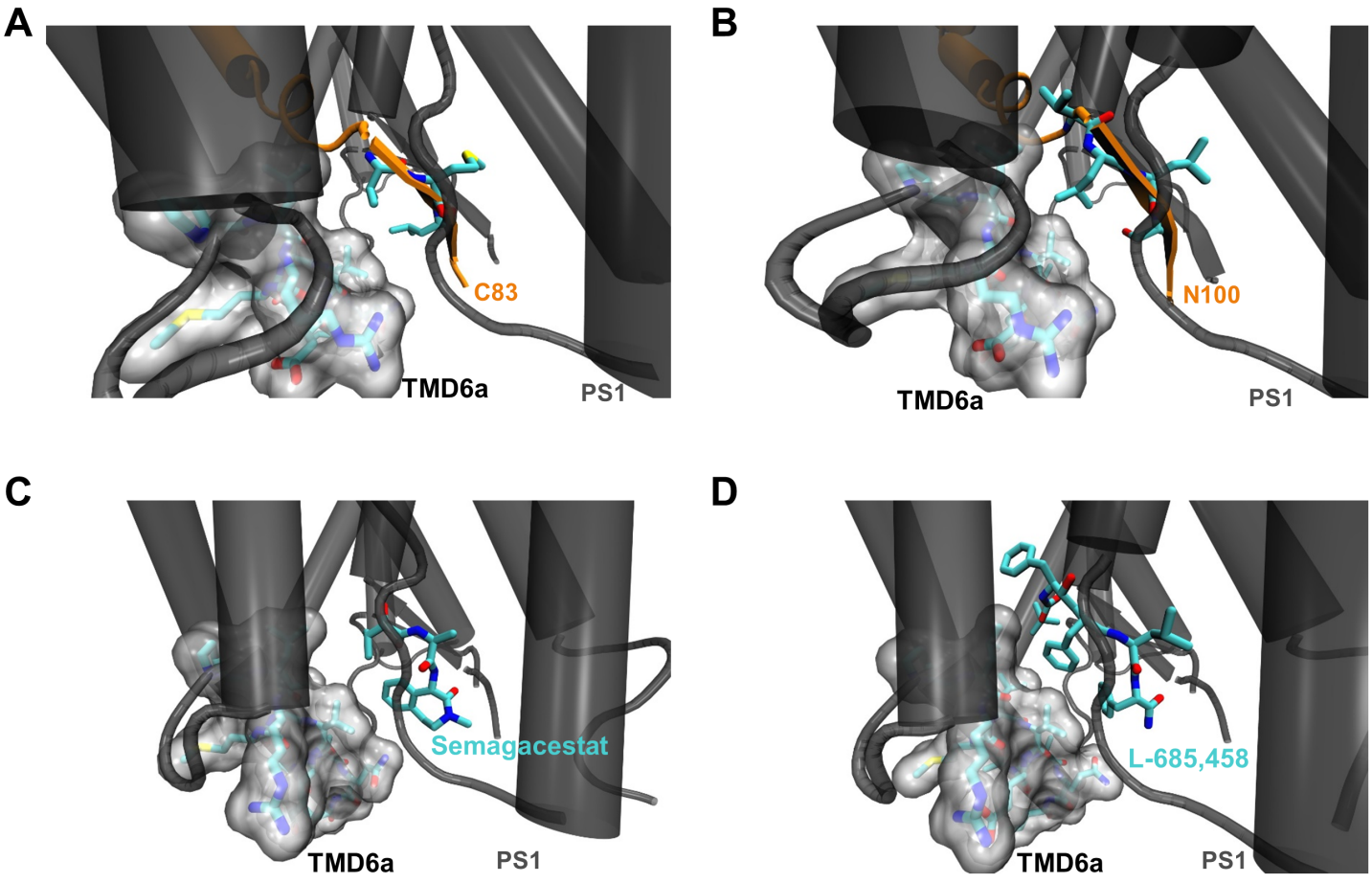

Figure 6 – figure supplement 1

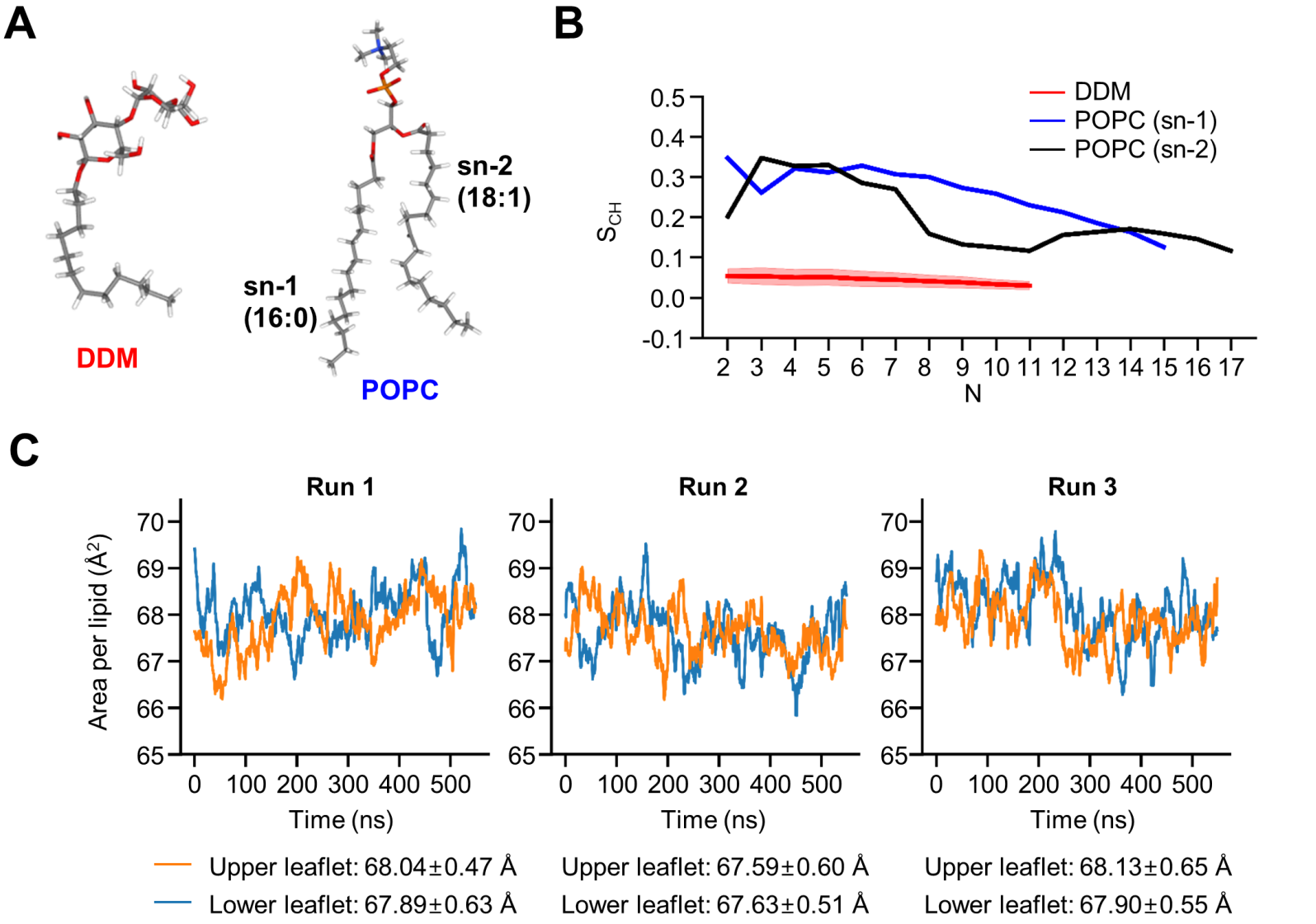

Figure 6 – figure supplement 2

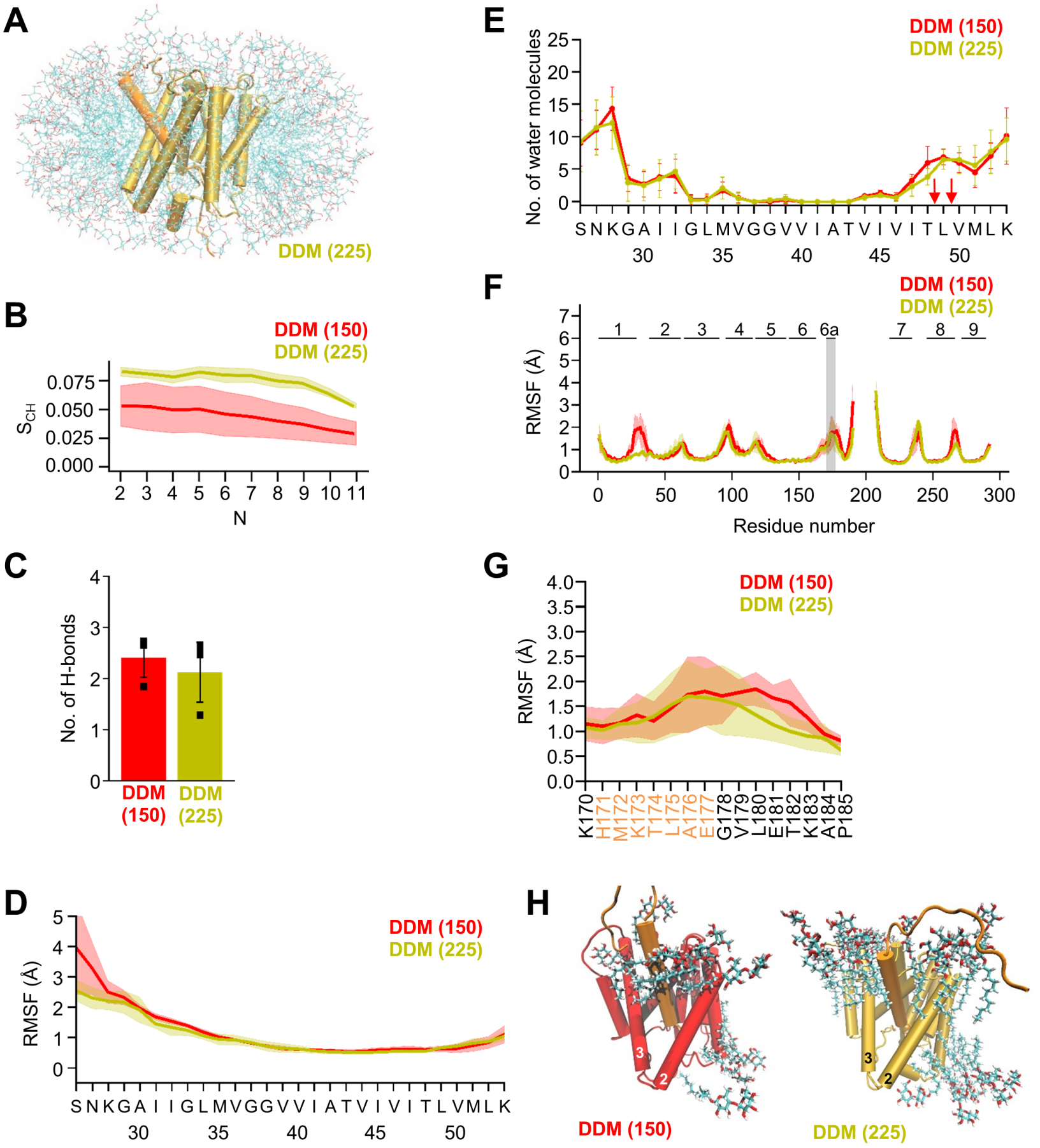

Figure 6 – figure supplement 3

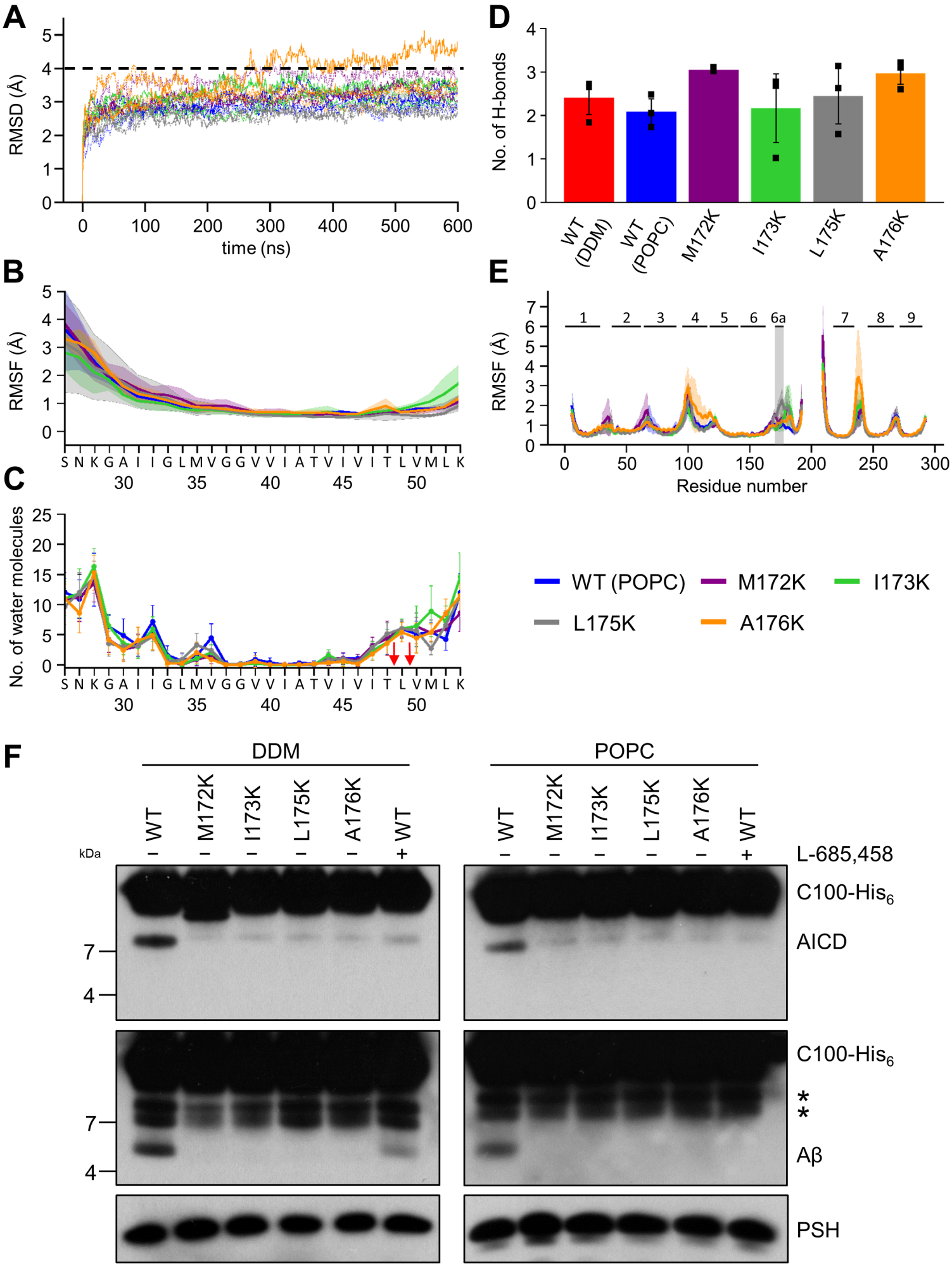
A
RMSD (Å)
time (ns)
B
RMSF (Å)
S N K G A I I G L M V G G V V I A T V I V I T L V M L K
30 35 40 45 50
C
No. of water molecules
S N K G A I I G L M V G G V V I A T V I V I T L V M L K
30 35 40 45 50
D
No. of H-bonds
WT (DDM)
WT (POPC)
M172K
I173K
L175K
A176K
E
RMSF (Å)
1 2 3 4 5 6 6a 7 8 9
Residue number
WT (POPC)
M172K
I173K
L175K
A176K
F
DDM
POPC
- WT
- M172K
- I173K
- L175K
- A176K
+ WT
kDa
7
4
L-685,458
C100-His6
AICD
C100-His6
**
Aβ
PSH

Figure 7

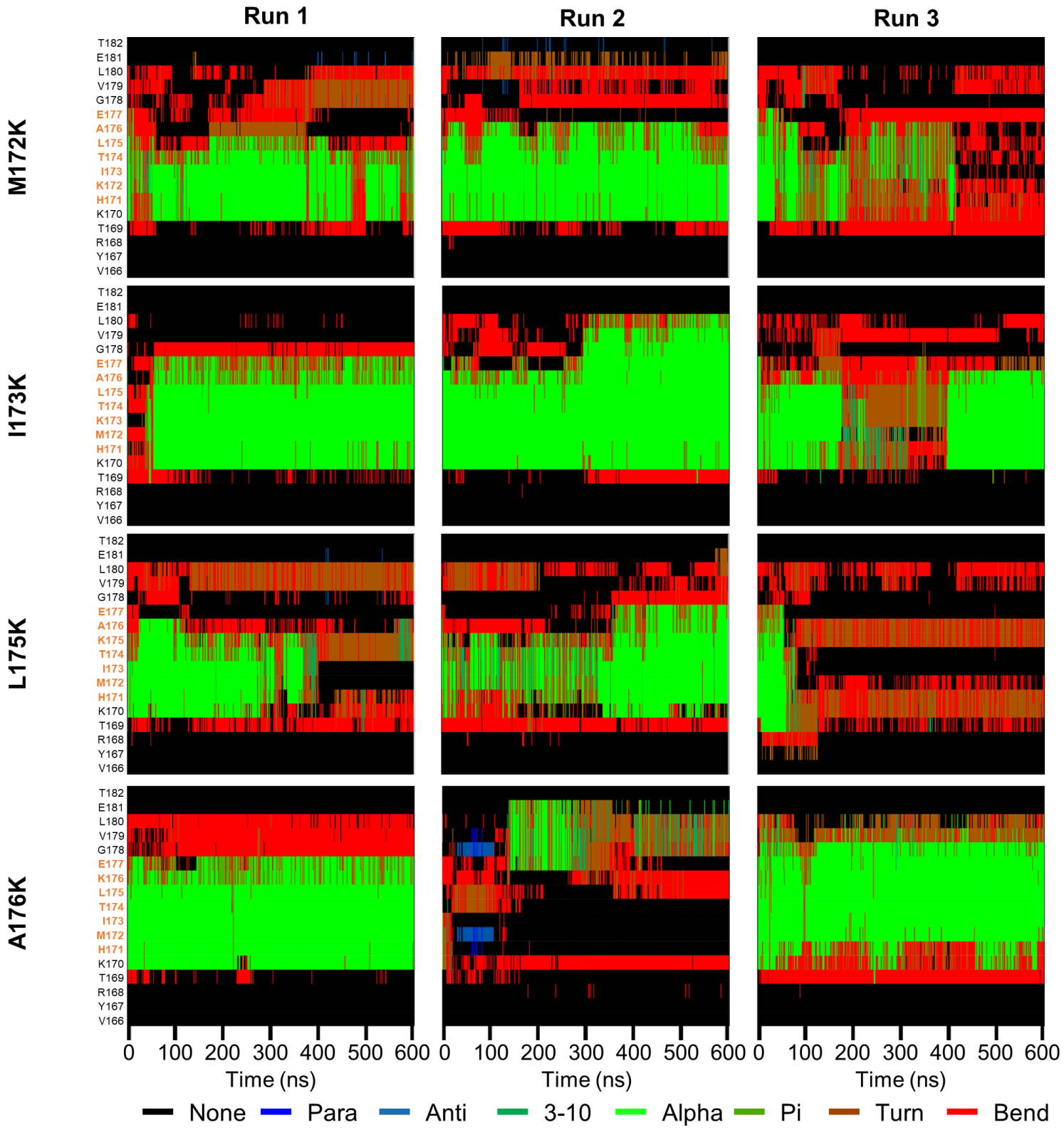

Figure 7 – figure supplement 1

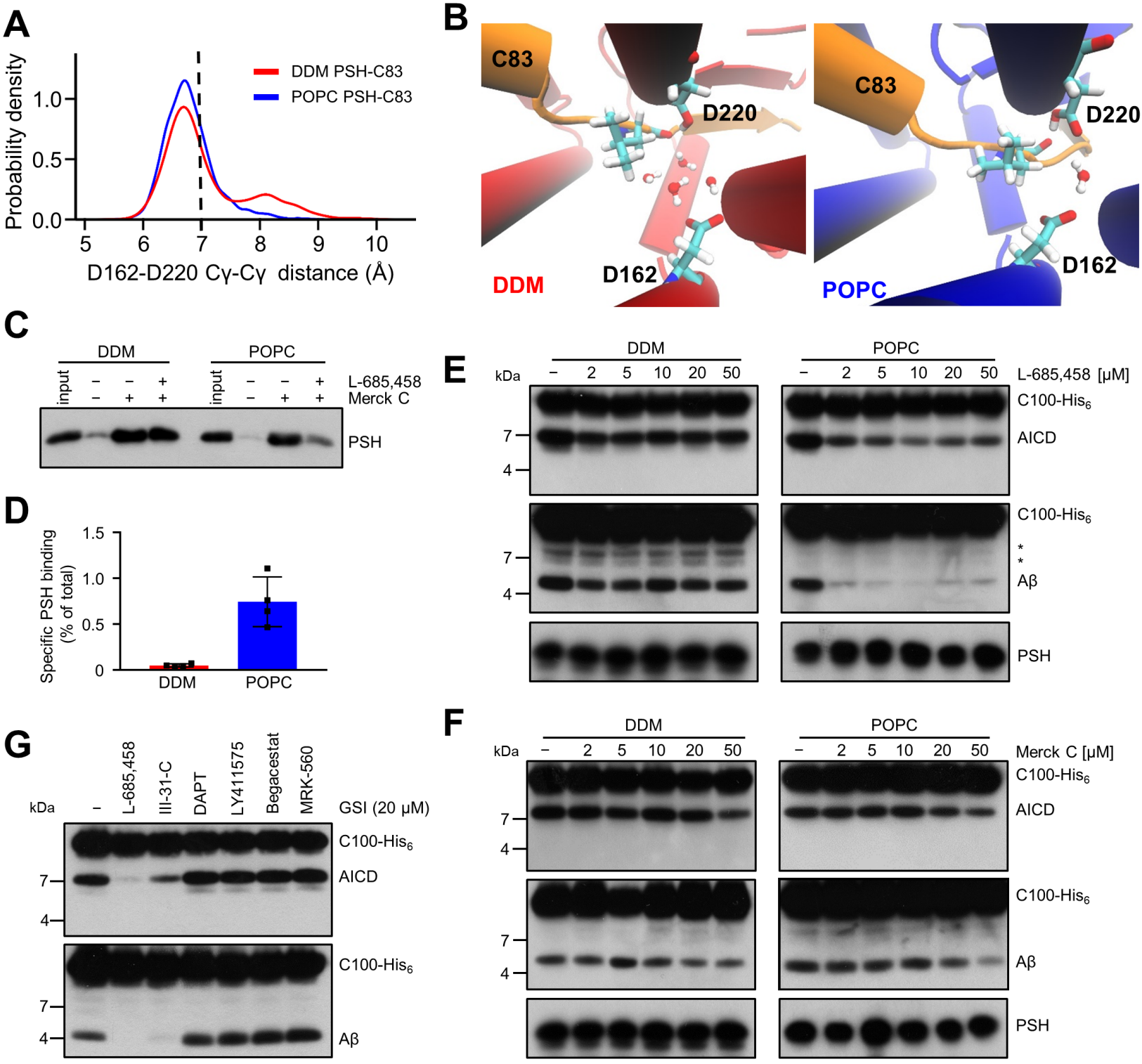
A
Probability density
1.0
0.5
0.0
5
6
7
8
9
10
D162-Dα Cγ-Cγ distance (Å)
DDM PSH-C83
POPC PSH-C83
B
C83
D220
D162
DDM
C83
D220
D162
POPC
C
DDM
POPC
input
L-685,458
Merck C
PSH
D
Specific PSH binding (% of total)
1.5
1.0
0.5
0
DDM
POPC
E
DDM
POPC
kDa
L-685,458 [μM]
C100-His6
AICD
Aβ
PSH
F
DDM
POPC
kDa
Merck C [μM]
C100-His6
AICD
Aβ
PSH
G
kDa
L-685,458
III-31-C
DAPT
LY411575
Begacestat
MRK-560
GSI (20 μM)
C100-His6
AICD
Aβ

Figure 8

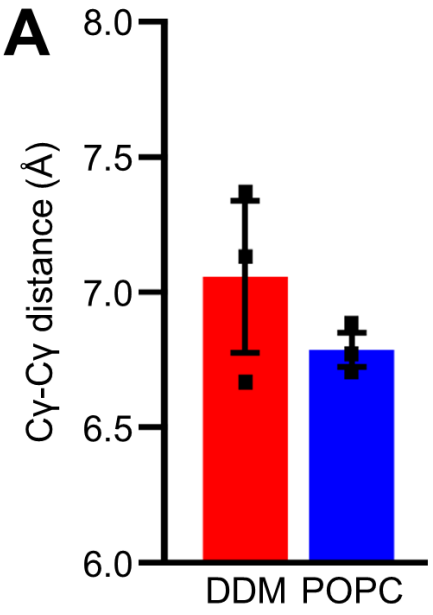

B

Frequency of Cγ-Cγ distance below 7 Å	
DDM	POPC
63%	76%

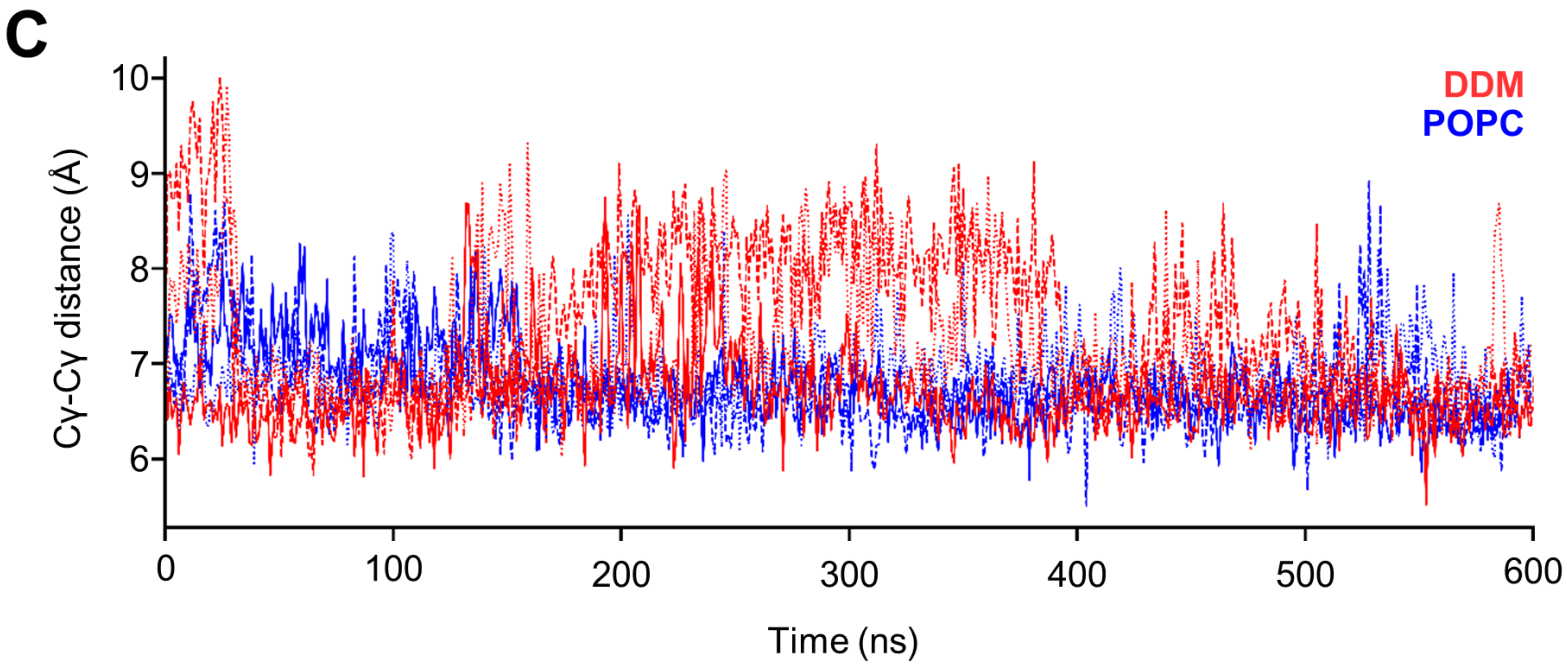

Figure 8 – figure supplement 1

A

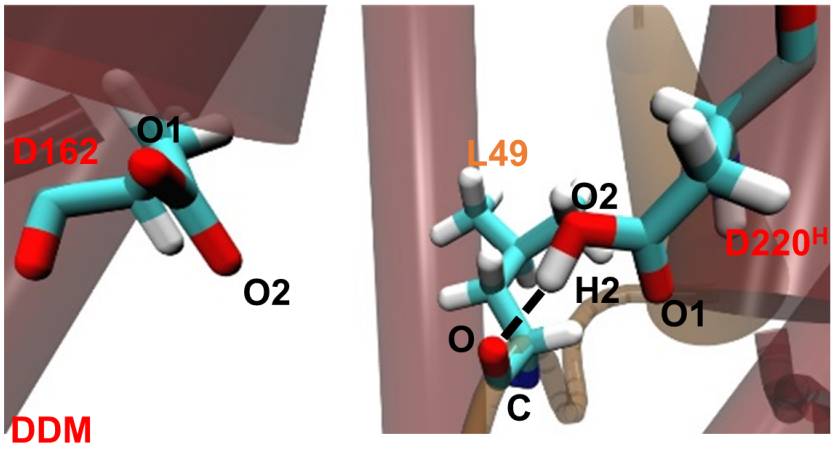

Distance (Å)	D162-O1	D162-O2	D220H-O1	D220H-O2	D220H-H2
L49-C	7.53	5.94	3.75	3.72	2.86
L49-O	6.64	5.29	3.46	2.86	1.93
D162-O1	0	0	9.10	7.07	6.85
D162-O2	0	0	8.21	6.43	5.99

B

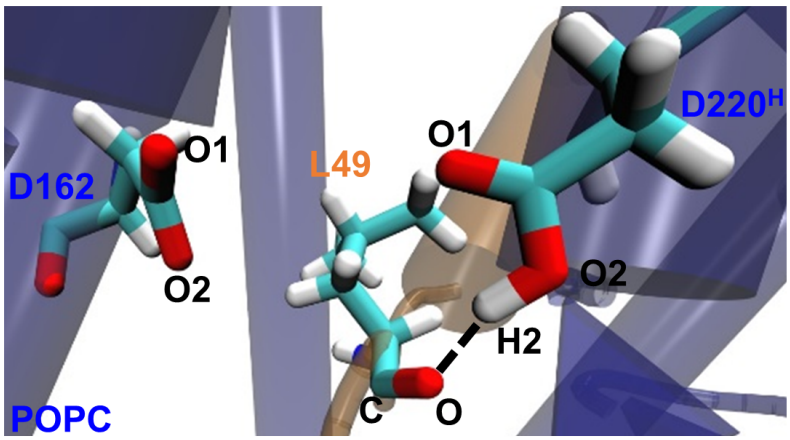

Distance (Å)	D162-O1	D162-O2	D220H-O1	D220H-O2	D220H-H2
L49-C	6.16	5.02	4.31	3.67	2.72
L49-O	6.19	5.44	3.75	2.69	1.77
D162-O1	0	0	4.88	6.57	6.14
D162-O2	0	0	5.29	6.61	5.93

Figure 8 – figure supplement 2

A L-685,458

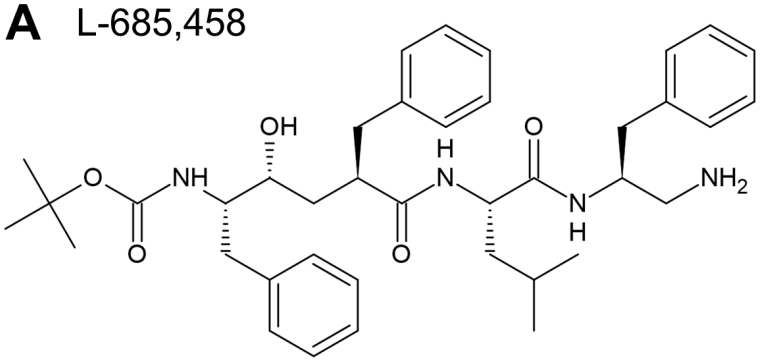

B III-31C

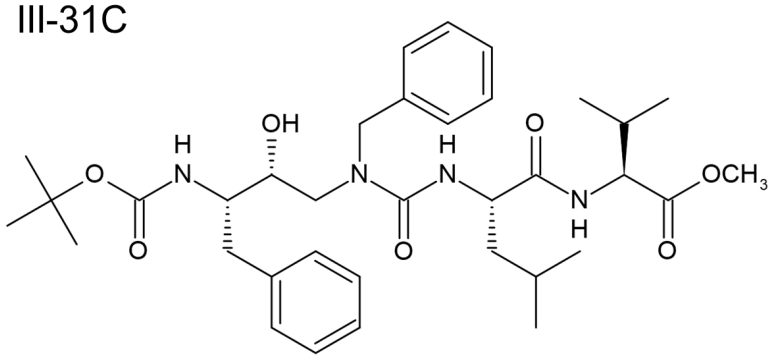

C DAPT

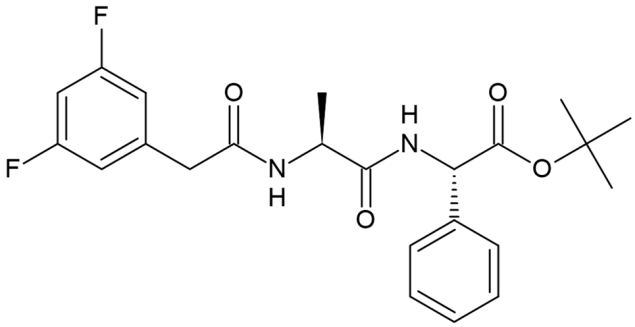

D LY411575

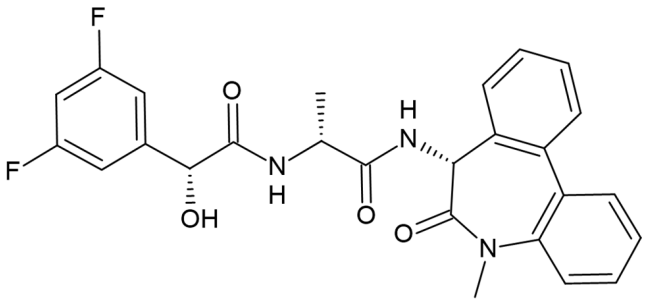

E Begacestat

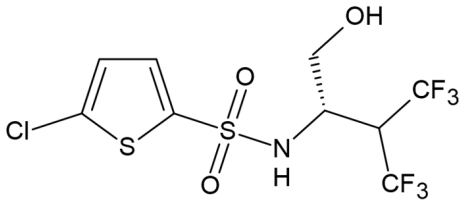

F MRK-560

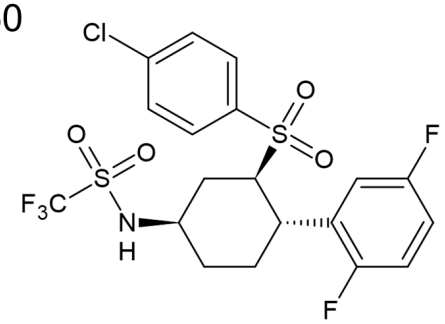

Figure 8 – figure supplement 3

A

PSH	Z-Ave (nm)
WT	47.93
M172K	10.68
I173K	34.42
L175K	20.91
A176A	29.07
A213P	13.47
F214P	13.49
V215P	19.41
Δ213-216	52.59
Δ213-217	11.10

B

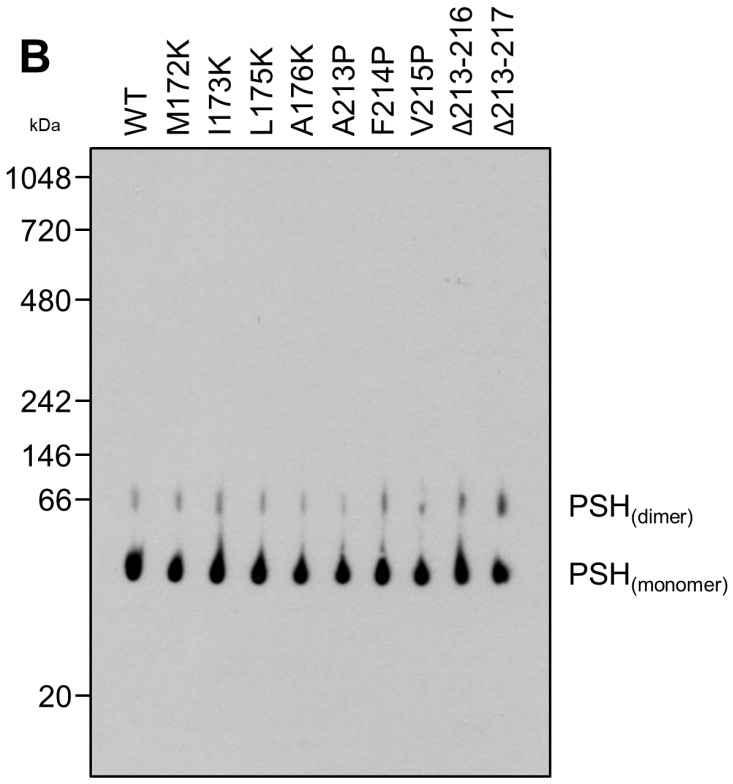

C

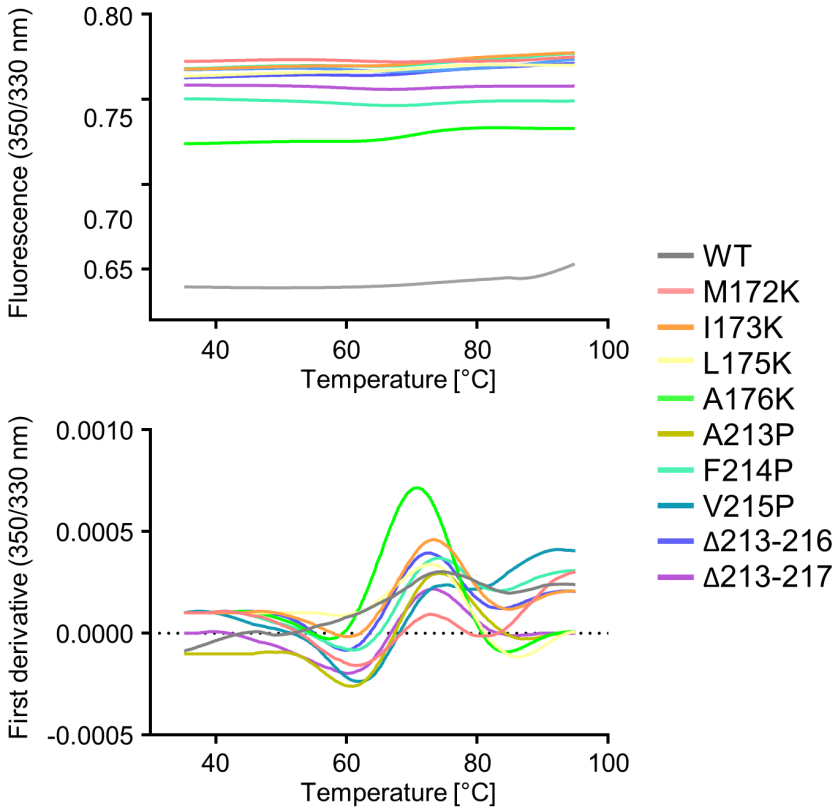

PSH	WT	M172K	I173K	L175K
T_i [°C]	74.255	72.293	73.440	72.232

PSH	A176K	A213P	F214P	V215P
T_i [°C]	70.573	73.923	73.198	73.319

PSH	Δ213-216	Δ213-217
T_i [°C]	71.987	72.745

Appendix 1 – figure 1